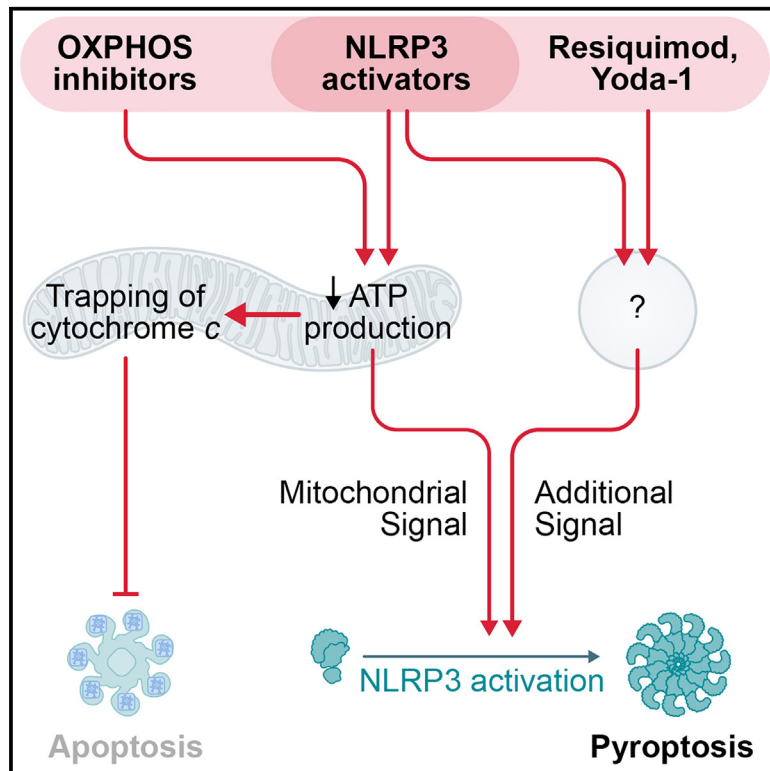# Immunity

Acute suppression of mitochondrial ATP production prevents apoptosis and provides an essential signal for NLRP3 inflammasome activation

Graphical abstract

Authors

Benedikt S. Saller, Svenja Wöhrle, Larissa Fischer, ..., Martin Schwemmle, Christina J. Groß, Olaf Groß

Correspondence

olaf.gross@uniklinik-freiburg.de

In brief

Mitochondria control metabolism, cell death, and innate immunity, yet their reciprocal mechanistic connections are elusive, as is the conserved physiological function of the NLRP3 inflammasome. Saller et al. reveal that inhibition of mitochondrial ATP production and of apoptosis are common effects of NLRP3 activators, suggesting that it evolved for their sensing.

Highlights

- NLRP3 inflammasome activators commonly suppress apoptosis upstream of NLRP3

- NLRP3 activators block mitochondrial ATP production (OXPHOS) by different mechanisms

- OXPHOS inhibition causes crista junction closure and retention of cytochrome *c*

- In addition to OXPHOS inhibition, NLRP3 activation requires a second activating signal

 CelPress

Article

Acute suppression of mitochondrial ATP production prevents apoptosis and provides an essential signal for NLRP3 inflammasome activation

Benedikt S. Saller,[1,2] Svenja Wöhrle,[1,3,33] Larissa Fischer,[1,3,33] Clara Dufossez,[1,3,33] Isabella L. Ingerl,[1,33]
Susanne Kessler,[4] Maria Mateo-Tortola,[5] Oliver Gorka,[1] Felix Lange,[6,7] Yurong Cheng,[8] Emilia Neuwirt,[1,2]
Adinarayana Marada,[9] Christoph Koentges,[1] Chiara Urban,[1] Philipp Aktories,[1,2,3] Peter Reuther,[4] Sebastian Giese,[4]

(Author list continued on next page)

[1]Institute of Neuropathology, Faculty of Medicine, Medical Center, University of Freiburg, Freiburg, Germany
[2]Signalling Research Centres BIOSS and CIBSS, University of Freiburg, Freiburg, Germany
[3]Faculty of Biology, University of Freiburg, Freiburg, Germany
[4]Institute of Virology, Faculty of Medicine, Medical Center, University of Freiburg, Freiburg, Germany
[5]Department of Innate Immunity, Institute of Immunology, University of Tübingen, Tübingen, Germany
[6]Research Group Mitochondrial Structure and Dynamics, Department of NanoBiophotonics, Max Planck Institute for Multidisciplinary Sciences, Göttingen, Germany
[7]Clinic for Neurology, University Medical Center of Göttingen, Göttingen, Germany
[8]Institute of Genetic Epidemiology, Faculty of Medicine, Medical Center, University of Freiburg, Freiburg, Germany
[9]Institute of Biochemistry and Molecular Biology, ZBMZ, Faculty of Medicine, University of Freiburg, Freiburg, Germany
[10]Institute of Medical Microbiology and Hygiene, Faculty of Medicine, Medical Center, University of Freiburg, Freiburg, Germany
[11]Gottfried Schatz Research Center, Molecular Biology and Biochemistry, Medical University of Graz, Graz, Austria
[12]Veterinary Physiological Chemical Institute, Faculty of Veterinary Medicine, University of Leipzig, Leipzig, Germany
[13]The Walter and Eliza Hall Institute of Medical Research, The Department of Medical Biology, University of Melbourne, Parkville, VIC, Australia
[14]Department of Developmental Immunology, Max Planck Institute of Immunobiology and Epigenetics, Freiburg, Germany
[15]Internal Medicine IV, Faculty of Medicine, Medical Center, University of Freiburg, Freiburg, Germany
[16]Institute of Clinical Neuroimmunology, University Hospital, Ludwig-Maximilians Universität München, Munich, Germany
[17]Biomedical Center (BMC), Faculty of Medicine, Ludwig-Maximilians Universität München, Martinsried, Germany
[18]Institute of Neuronal Cell Biology, Technical University of Munich, Munich, Germany
[19]Institute for Molecular Medicine and Cell Research, ZBMZ, Faculty of Medicine, University of Freiburg, Freiburg, Germany

(Affiliations continued on next page)

SUMMARY

How mitochondria reconcile roles in functionally divergent cell death pathways of apoptosis and NLRP3 inflammasome-mediated pyroptosis remains elusive, as is their precise role in NLRP3 activation and the evolutionarily conserved physiological function of NLRP3. Here, we have shown that when cells were challenged simultaneously, apoptosis was inhibited and NLRP3 activation prevailed. Apoptosis inhibition by structurally diverse NLRP3 activators, including nigericin, imiquimod, extracellular ATP, particles, and viruses, was not a consequence of inflammasome activation but rather of their effects on mitochondria. NLRP3 activators turned out as oxidative phosphorylation (OXPHOS) inhibitors, which we found to disrupt mitochondrial cristae architecture, leading to trapping of cytochrome *c*. Although this effect was alone not sufficient for NLRP3 activation, OXPHOS inhibitors became triggers of NLRP3 when combined with resiquimod or Yoda-1, suggesting that NLRP3 activation requires two simultaneous cellular signals, one of mitochondrial origin. Therefore, OXPHOS and apoptosis inhibition by NLRP3 activators provide stringency in cell death decisions.

INTRODUCTION

Inflammasomes are cytoplasmic danger-sensing complexes, consisting of an oligomerized sensor protein and the protease

caspase-1, typically connected by multimers of the adapter protein ASC.[1,2] Upon inflammasome formation, caspase-1 cleaves not only pro-interleukin (IL)-1β and pro-IL-18 to generate the bioactive cytokines but also the pore-forming protein

Susanne Kirschnek,[10] Carolin Mayer,[10] Johannes Pilic,[11] Hugo Falquez-Medina,[9,12] Aline Oelgeklaus,[9,12] Veerasikku Gopal Deepagan,[13] Farzaneh Shojaee,[13] Julia A. Zimmermann,[14] Damian Weber,[2,15] Yi-Heng Tai,[16,17,18] Anna Crois,[3,19] Kevin Ciminski,[4] Remi Peyronnet,[20] Katharina S. Brandenburg,[1] Gang Wu,[21] Ralf Baumeister,[2,9,21] Thomas Heimbucher,[21] Marta Rizzi,[2,22,23] Dietmar Riedel,[24] Martin Helmstädter,[25] Joerg Buescher,[26] Konstantin Neumann,[27] Thomas Misgeld,[18,28,29] Martin Kerschensteiner,[16,17,29] Peter Walentek,[2,15] Clemens Kreutz,[2,30] Ulrich Maurer,[2,19] Angelika S. Rambold,[14] James E. Vince,[13] Frank Edlich,[9,12] Roland Malli,[11] Georg Häcker,[10] Katrin Kierdorf,[1,2] Chris Meisinger,[2,9] Anna Köttgen,[2,8] Stefan Jakobs,[6,7,31] Alexander N.R. Weber,[5,32] Martin Schwemmle,[4] Christina J. Groß,[2] and Olaf Groß[1,2,34,*]

[20]Institute for Experimental Cardiovascular Medicine, Faculty of Medicine, University Heart Center Freiburg – Bad Krozingen, University of Freiburg, Freiburg, Germany
[21]Bioinformatics and Molecular Genetics, Faculty of Biology, University of Freiburg, Freiburg, Germany
[22]Department of Rheumatology and Clinical Immunology and Center for Chronic Immunodeficiency, Faculty of Medicine, Medical Center, University of Freiburg, Freiburg, Germany
[23]Division of Clinical and Experimental Immunology, Institute of Immunology, Center for Pathophysiology, Infectiology and Immunology, Medical University of Vienna, Vienna, Austria
[24]Laboratory for Electron Microscopy, Max Planck Institute for Multidisciplinary Sciences, Göttingen, Germany
[25]EMcore, Internal Medicine IV, Faculty of Medicine, Medical Center, University of Freiburg, Freiburg, Germany
[26]Metabolomics and FACS Core Facilities, Max Planck Institute of Immunobiology and Epigenetics, Freiburg, Germany
[27]Institute of Clinical Chemistry, Hannover Medical School, Hannover, Germany
[28]German Center for Neurodegenerative Diseases (DZNE), Munich, Germany
[29]Munich Cluster for Systems Neurology (SyNergy), Munich, Germany
[30]Institute of Medical Biometry and Statistics, Faculty of Medicine, Medical Center, University of Freiburg, Freiburg, Germany
[31]Fraunhofer Institute for Translational Medicine and Pharmacology ITMP, Translational Neuroinflammation and Automated Microscopy TNM, Göttingen, Germany
[32]Clusters of Excellence EXC-2180 (iFIT) and -2124 (CMFI), University of Tübingen, Tübingen, Germany
[33]These authors contributed equally
[34]Lead contact
*Correspondence: olaf.gross@uniklinik-freiburg.de
https://doi.org/10.1016/j.immuni.2024.10.012

gasdermin-D (GSDMD) that then inserts into cellular membranes, leading to inflammatory IL-1 release and pyroptosis.[3] Of the inflammasome-nucleating sensors, NLRP3 stands out not only for its sheer range of endogenous and exogenous activators but also for its role in immunopathology in a wide variety of diseases. Although NLRP3 is triggered by some microbial pathogens, it is unclear what protective role justifies the conservation of NLRP3 despite its penchant to instigate pathological inflammation.[4,5] NLRP3 is indirectly triggered in response to cellular stress signals initiated by its activators.[6,7] Although its precise activation mechanism has yet to be resolved, mitochondria have been implicated in several studies.[6–11] Potassium (K^+) efflux has been previously thought to be the common trigger of NLRP3 activation,[12] yet we and others have shown that NLRP3 activation is in principle possible in the absence of K^+ efflux.[8,13–15] Other effects of its activators, including its relocalization to the endosomal or Golgi compartment, have been implicated in NLRP3 triggering.[6,7,16–19] Thus, NLRP3 seems to sense multiple signals for its activation, but it remains unclear what specific danger information they convey and what the minimal requirements for NLRP3 activation are. Preceding activation, NLRP3 is also regulated at the transcriptional and post-translational levels in a process called priming.[20]

Apart from their bioenergetic and metabolic functions, mitochondria also have a central role in the intrinsic apoptosis pathway.[21] In this pathway, mitochondria release cytochrome *c* (an integral component of the electron transport chain [ETC]), from cristae stores to the cytoplasm, where it triggers apoptosome formation. Similar to the inflammasome, the apoptosome consists of a sensor and a protease, with APAF-1 sensing cytochrome *c* in the cytoplasm and caspase-9 cleaving caspase-3 to

initiate apoptosis.[21] In stark contrast to pyroptosis, membrane integrity is generally preserved during apoptosis, rendering it less immunogenic.[21] Mitochondria are therefore at a crux in cell death decision-making,[22] and the outcome of such decisions can have fundamental consequences for the surrounding tissue in achieving a balance between robust, protective immunity and avoiding tissue damage to maintain tissue homeostasis.

Here, we sought to elucidate the role of mitochondria in decision-making between NLRP3 activation and apoptosis. Our results shed light not only on the cross-talk between these cell death pathways but also on the activating signals and potential physiological function of NLRP3.

RESULTS

Nigericin broadly suppresses intrinsic apoptosis independently of NLRP3 and pyroptosis

We simultaneously triggered mitochondrial apoptosis and NLRP3 in primed macrophages using raptinal, a fast-acting apoptosis inducer,[23] and nigericin, a standard NLRP3 activator.[24] When challenged with both at the same time, the cells still released IL-1β and executed pyroptosis, consistent with caspase-1 cleavage being unaltered (Figures 1A, 1B, S1A, and S1B). By contrast, nigericin co-treatment completely prevented raptinal-induced cleavage of apoptosis executioner caspase-3.[21] Nigericin inhibited raptinal-induced caspase-3 cleavage in any myeloid cell type tested, including primary murine microglia and human monocyte-derived macrophages (Figures 1B–1E and S1B–S1D). This effect of nigericin displayed a similar dose dependency as its ability to trigger IL-1β release (Figures S1E and S1F). A simple explanation
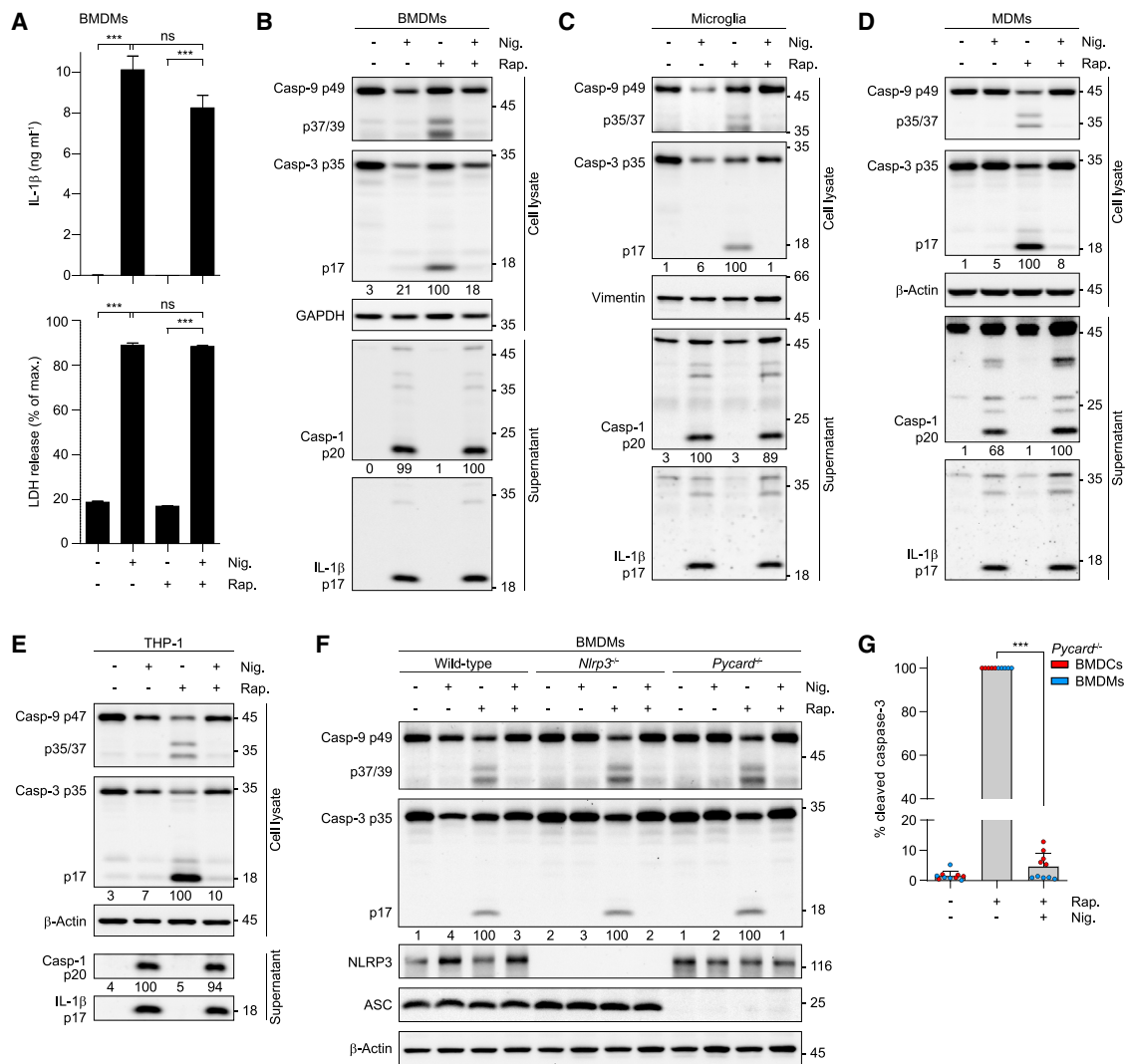
Figure 1. Nigericin inhibits intrinsic apoptosis independent of NLRP3 and pyroptosis

(A–G) Indicated murine wild-type or inflammasome-deficient (A–C, F, and G) and human (D and E) cell types were lipopolysaccharide (LPS)-primed and treated with nigericin (nig.), raptinal (rap.), or combinations thereof for 1–2 h.

(A) IL-1β and LDH were quantified from cell-free supernatants by ELISA or a colorimetric assay.

(B–F) Cleavage of caspase-1, -3, and -9, and IL-1β was determined by immunoblotting of cell lysates or cell-free supernatants. Specific cleavage products were quantified and are depicted as percentage relative to the condition yielding the strongest signal (within the respective genotype) after normalization to the loading control for cell lysates. Numbers under protein bands indicate relative quantified signal intensities.

(G) After LPS priming and treatment for 1.5 h (bone marrow-derived dendritic cells [BMDCs]) or 2 h (bone marrow-derived macrophages [BMDMs]), caspase-3 cleavage was quantified from immunoblots and is depicted from 10 independent experiments as percent of the raptinal-only condition.

For statistical analysis, METs (A) or a paired t test (G) were performed. Data are depicted as mean ±SD (A and G) and are representative of two (D) or at least three experiments (A, B, E, and F). See also Figure S1.

Significance levels are denoted as *$p < 0.05$, **$p < 0.01$, ***$p < 0.001$, and ns for not significant.

would have been different cell death kinetics, i.e., that rapid pyroptotic lysis precedes and precludes apoptosis. However, nigericin-induced pyroptosis and raptinal-induced apoptosis had comparable kinetics with 50% of phosphatidylserine exposure (a hallmark of either cell death modality[25]) following ~45 min of treatment (Figure S1G). Consistent with these kinetics, nigericin-induced IL-1β production was significantly reduced when raptinal was added 45 min before nigericin and largely diminished at 1 h of preincubation (Figure S1H). This correlated with the onset of full caspase-3 activity and

the degradation of GSDMD[26,27] and pro-IL-1β after 1 h of raptinal treatment (Figure S1I). Conversely, suppression of caspase-3 was still observed even when adding nigericin 20 min after raptinal (Figure S1J). Cytoplasmic DNA, a trigger of the AIM2 inflammasome, did not suppress raptinal-induced caspase-3 cleavage (Figures S1K and S1L). Nigericin-induced suppression of caspase-3 cleavage and also inhibition of phosphatidylserine exposure were still observed in cells deficient in the inflammasome components NLRP3 or ASC (encoded by *Pycard*) that are essential for caspase-1 activation[24]
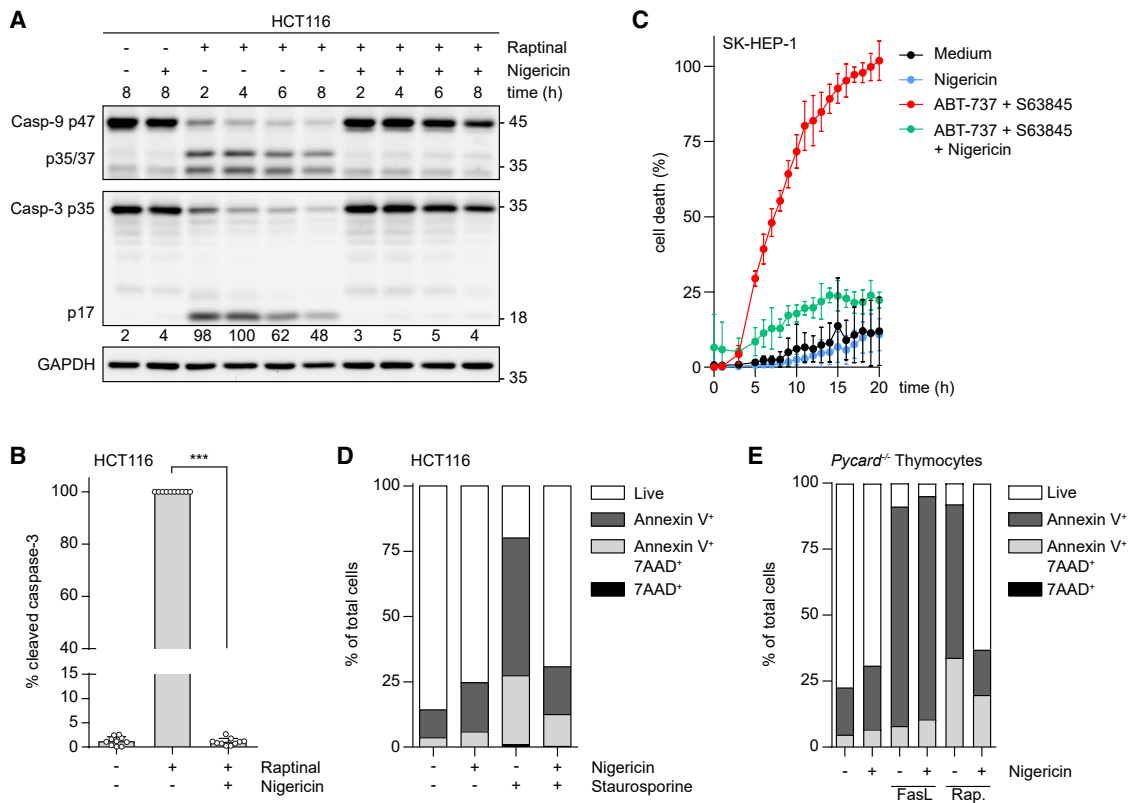
Figure 2. Nigericin inhibits intrinsic apoptosis in diverse cell types
(A–E) Indicated human (A–D) and primary murine (E) cell types were treated as indicated.
(A) Caspase cleavage was determined as in Figures 1B–1F.
(B) Quantified immunoblots of 10 independent experiments (treatment for 1.5 or 2 h) are depicted as percent of the raptinal-only condition.
(C) Live and dead cells were detected using the IncuCyte imaging system.
(D and E) After treatment for 20 h (D) or 1 h (E), cell death was assessed by flow cytometry.
For statistical analysis, a paired t test was performed (B). Data are depicted as mean ± SD (B and C) and are representative of two (E) or at least three experiments (A, C, and D). See also Figure S2.
Significance levels are denoted as *$p < 0.05$, **$p < 0.01$, ***$p < 0.001$, and ns for not significant.

(Figures 1F, 1G, S1E, S1F, S1J, S1K, S1M, and S1N). Collectively, these results suggest that nigericin suppresses apoptosis but that this was not a consequence of inflammasome activation or pyroptosis induction.

Nigericin-induced suppression of apoptosis was not only observed in (inflammasome-competent or genetically deficient) myeloid cells (Figures 1 and S1) but also in any other non-inflammasome-competent cell type of human, murine, or simian origin tested (Figures 2A, 2B, S2A, and S2B). HCT116 and HeLa cells (Figures 2A and S2A) are standard tools for apoptosis and mitochondria research,[23,28–31] which we choose for further studies on the mechanisms engaged by nigericin. Apoptosis suppression by nigericin was observed even after extended co-stimulation with raptinal and nigericin (Figure 2A) and also prevented the typical "blebbing" apoptotic morphology (Figure S2C). Nigericin also suppressed cell death in response to other activators of the intrinsic apoptosis pathway, including BH3 mimetics[32–34] and staurosporine[21] (Figures 2C, 2D, and S2D). To confirm that the effect of nigericin on apoptosis was specific for the intrinsic pathway, we treated primary murine thymocytes with Fas-ligand to trigger

the caspase-8-dependent extrinsic apoptosis pathway[35] and observed that nigericin did not suppress extrinsic apoptosis (Figure 2E).

Nigericin prevents cytochrome c release and disrupts mitochondrial cristae morphology

We next sought to characterize the mechanism by which nigericin inhibits intrinsic apoptosis. Mitochondrial cytochrome c release is central for the intrinsic apoptosis pathway (Figure S2E).[21] Nigericin treatment led to strong and sustained suppression of cytochrome c release into the cytoplasm (Figure 3A). It prevented cleavage of caspase-3 when added after raptinal only up to such times when cytochrome c was not yet released from mitochondria, suggesting that cytochrome c release is the point-of-no return for apoptosis (Figures S3A and S3B). Cytochrome c is primarily localized within mitochondrial cristae, where it associates with the inner mitochondrial membrane lipid cardiolipin and ETC complexes III and IV.[36] Its dissociation and passage through crista junctions into the intermembrane space are thought to make it available for release (Figure S2E).[37,38] While most apoptosis inducers trigger mitochondrial outer
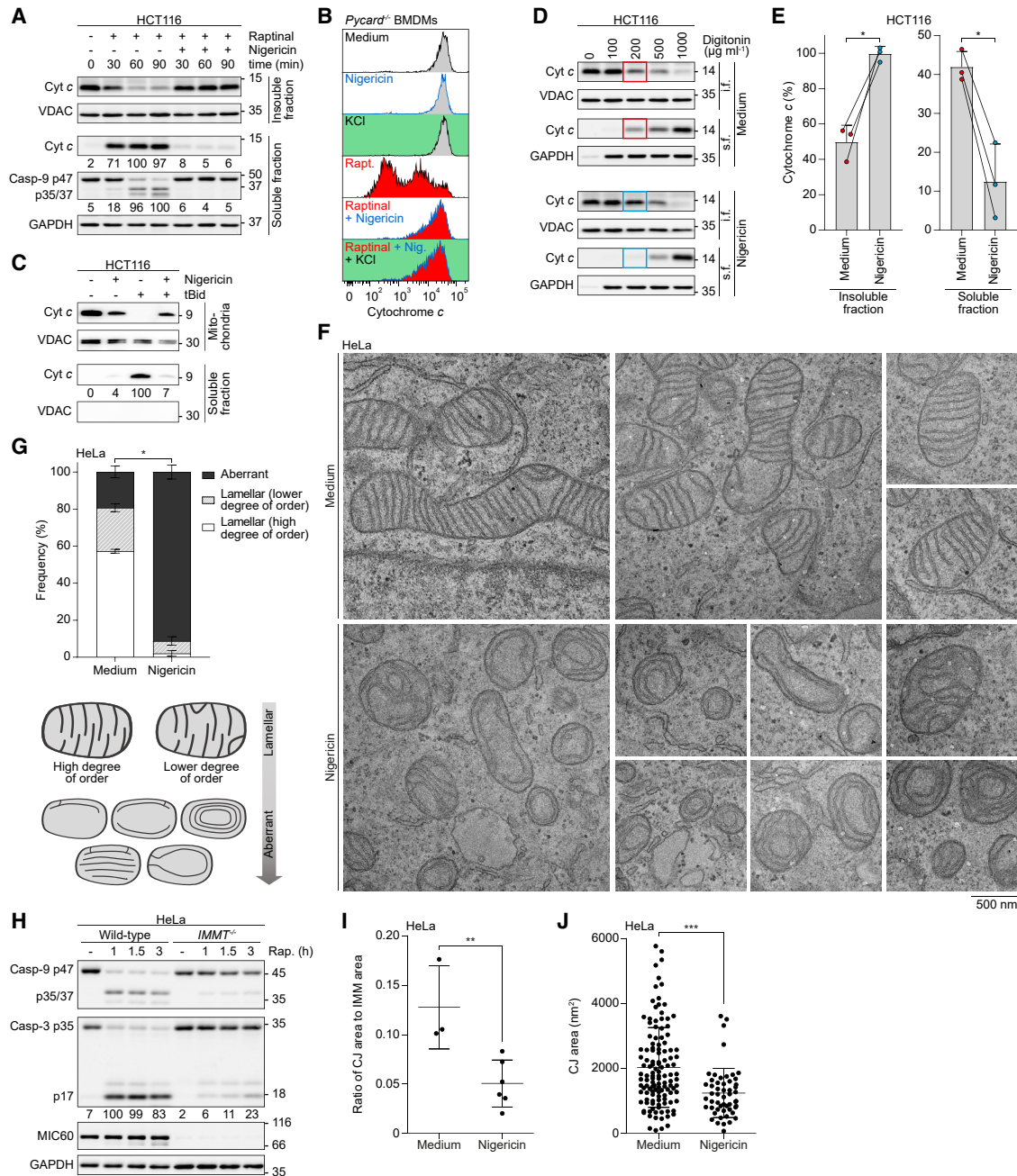
Figure 3. Nigericin prevents cytochrome *c* release and disrupts cristae morphology

(A–J) Indicated human or (A and C–J) or murine (B) wild-type or gene-deficient cell types were treated as indicated.

(A) Following digitonin permeabilization, cells were fractionated into a mitochondria-containing insoluble and a soluble fraction. Immunoblot signals were quantified as in Figures 1B–1F and are depicted as percentage relative to the strongest signal after normalization to the loading control.

(B) After treatment for 1.5 h, cytochrome *c* release was assessed by flow cytometry.

(C) Cytochrome *c* release from isolated mitochondria after 10 min of treatment was quantified from immunoblots and depicted as percentage relative to the strongest signal.

(D and E) After treatment for 0.5 h and permeabilization with the indicated concentrations of digitonin, cells were fractionated into a mitochondria-containing insoluble (i.f.) and a soluble fraction (s.f.). Cytochrome *c* release was quantified from immunoblots (D). Corrected intensities for cytochrome *c* at 200 μg mL^{-1} digitonin (red and blue boxes) are shown in percent relative to maximum. Pooled data of three independent experiments are depicted (E), of which one is shown in (D).

(F and G) After treatment with for 0.5 h, mitochondrial morphology was assessed by TEM (F) and categorized (G).

(H) Caspase cleavage was determined as in Figures 1B–1F.

(legend continued on next page)

membrane permeabilization via BAX and BAK pores,[21] raptinal induces cytochrome *c* release independently of BAX and BAK[23,28] and suppression of raptinal-induced apoptosis was intact in BAX^{−/−}BAK^{−/−} cells (Figure S3C). In contrast to NLRP3 activation by nigericin,[12] prevention of caspase-3 cleavage and of cytochrome *c* release was independent of K^{+} efflux from cells (Figures 3B and S3D). This suggests that nigericin suppressed apoptosis upstream of cytochrome *c* release, probably via effects on mitochondria.

To test such a direct effect, we isolated mitochondria from human and murine cells and treated them with recombinant tBID, a cell-endogenous apoptosis inducer.[21] Nigericin prevented tBID-induced cytochrome *c* release (Figures 3C and S3E). To assess if nigericin affects cytochrome *c* availability for release, we treated cells with a detergent at conditions that permeabilized only the outer but not the inner mitochondrial membrane (Figure S3F).[30] Even here, nigericin pre-treatment dampened cytochrome *c* release (Figures 3D and 3E), suggesting that it reduced its availability for release.

Changes in mitochondrial morphology might account for the suppression of cytochrome *c* release by mitochondria. To test this, we performed confocal and transmission electron microscopy. Nigericin induced mitochondrial fragmentation and prevented raptinal-induced late-stage mitochondrial swelling[39] (Figures S3G–S3I). Nigericin also caused a rapid rearrangement of cristae, including loss of lamellar organization, disruption of normal cristae orientation, and reduced frequency of crista junctions (Figures 3F and 3G). A similar cristae morphology has been observed in cells deficient for components of the MICOS complex that organizes crista junctions.[31] To elucidate if a loss of crista junctions directly affects apoptosis, we tested cells deficient for the MICOS component MIC60 (encoded by *IMMT*). In these, raptinal-induced caspase-3 cleavage was strongly impaired (Figure 3H). Indeed, similar to MICOS-deficient cells,[31] 3D reconstructions also showed a reduction in cristae junction density and individual area upon nigericin treatment (Figures 3I, 3J, and S3J). Therefore, our results are consistent with a model in which nigericin promotes cristae rearrangements with closure of crista junctions or fission of cristae from the inner boundary membrane, thereby trapping cytochrome *c* in the cristae lumen.

Uncouplers, including NLRP3-activating ionophores, inhibit apoptosis

We next asked how nigericin causes changes in mitochondrial morphology and performed untargeted metabolomics. After optimizing conditions (Figure S4A), we detected a total of 570 metabolites in (inflammasome-deficient) macrophages. Nigericin treatment at NLRP3-activating and apoptosis-inhibiting concentrations led to pronounced metabolic changes (Figures 4A, 4B, and S4B). The most strongly reduced were metabolites of *de novo* pyrimidine biosynthesis (carbamoyl aspartate, dihydroorotate, and orotate), directly derived from carbamoyl phos-

phate. Carbamoyl phosphate is synthesized in the regulated and irreversible step of pyrimidine biosynthesis from glutamine and bicarbonate, consuming two molecules of ATP. Phosphocreatine, shuttling ATP between the mitochondrial matrix and the cytosol,[10] was also depleted, while unphosphorylated purine bases were enriched. These observations were consistent with insufficient mitochondrial ATP production and the induction of compensatory mechanisms. Indeed, cellular ATP dropped substantially in macrophages in the presence of nigericin, especially when combined with the glycolysis inhibitor 2-DG (Figure 4C). Nigericin is a K^{+}/H^{+} antiporter that dissipates the mitochondrial proton gradient and thus uncouples mitochondrial respiration from oxidative phosphorylation (OXPHOS) in isolated mitochondria and also intact cells.[40] Indeed, many cation/proton ionophores have uncoupling activity.[41] We postulated that the uncoupling effect of nigericin might account for its pronounced impact on metabolism and directly compared its global influence on metabolism with that of FCCP,[42] a classical uncoupler and mobile proton carrier (see Figure S2E for reference of the mode-of-action of substances used herein). Principal-component analysis showed that nigericin and FCCP alter metabolism in the same direction along the major axes of variation (PC1 and PC2) in the metabolomics datasets (Figure 4D). The changes in mitochondrial morphology observed with FCCP were also similar to those induced by nigericin (Figure S4C). We therefore sought to determine if the ability of nigericin to inhibit apoptosis was connected to uncoupling and tested whether FCCP could also inhibit apoptosis. FCCP suppressed raptinal-induced cytochrome *c* release from mitochondria, caspase-3 processing, and phosphatidylserine exposure (Figures 4E, 4F, and S4D–S4F) in human and murine cells. Gramicidin as a well-established K^{+}/H^{+} ionophore and NLRP3 activator,[12] also suppressed raptinal-induced apoptosis (Figure S4G). We tested additional, chemically distinct K^{+}/H^{+} ionophores[43] that displayed uncoupling activity (Figure S4H). All of them, but not a calcium ionophore, also suppressed raptinal-induced apoptosis (Figures 4G, 4H, S4I, and S4J). Furthermore, the K^{+}/H^{+} ionophores had similar effects on mitochondrial morphology and cristae structure as those observed with nigericin (Figure S4K). Therefore, chemically diverse K^{+} and H^{+} ionophores with uncoupling activity suppressed intrinsic apoptosis.

Our data suggest that K^{+}/H^{+} ionophores inhibit apoptosis by causing changes in the mitochondrial cristae morphology that lead to trapping of cytochrome *c* within mitochondria. However, an additional effect of uncoupling agents that might also contribute to apoptosis inhibition is the reduction in mitochondrial ATP production itself. The established ATP-consuming steps of apoptosis occur downstream of cytochrome *c* release, when ATP is required in the cytoplasm, both for the execution phase downstream of caspase-3 activation and for activation of APAF-1 during the initiation of apoptosis.[44,45] However, in contrast to macrophages, neither FCCP nor nigericin alone reduced total cellular ATP in HCT116 cells (Figures 4C and 4I),

---

(I and J) After treatment for 0.5 h, crista junction (CJ) areas and the total inner mitochondrial membrane (IMM) area were assessed based on representative electron tomography reconstructions (see Figure S3I). The ratio of CJ to IMM area (I) or individual CJ areas (J) are depicted.

For statistical analysis, paired (E and G) and unpaired (I and J) t tests were performed. In (G), a difference in the aberrant group was assessed. Data are depicted as mean ± SD (E, G, I, and J) and are representative of two (F) or at least three independent experiments (A–D and H). See also Figure S3.

Significance levels are denoted as *$p < 0.05$, **$p < 0.01$, ***$p < 0.001$, and ns for not significant.

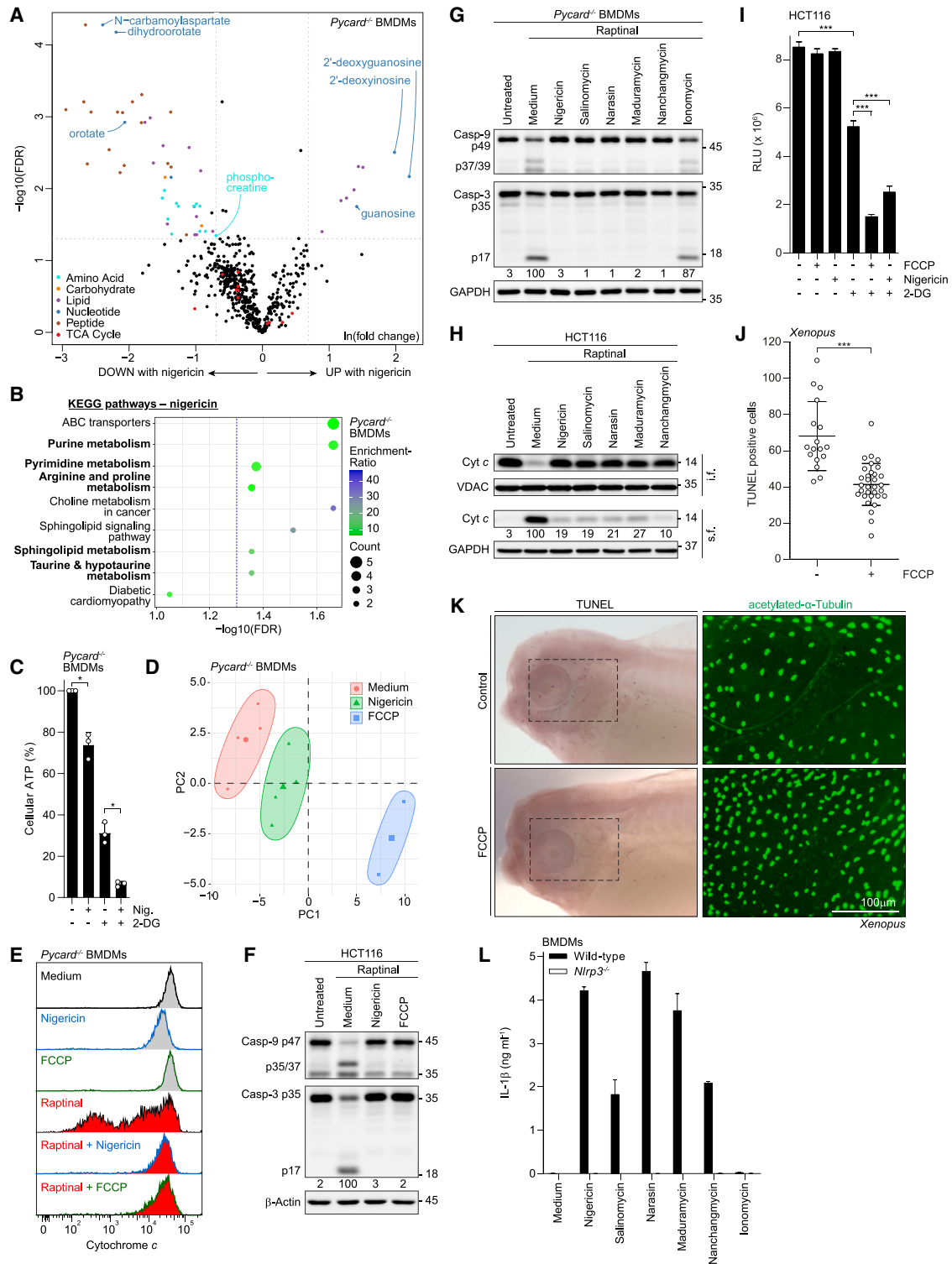**Figure 4. Inhibition of apoptosis by uncoupling H⁺ and K⁺ ionophores**

(A–I and L) Indicated murine wild-type or inflammasome-deficient (A–E, G, and L), or human (F, H, and I) cell types were treated as indicated.

(A and B) After LPS priming and treatment for 1 h, metabolites were extracted and measured by ultra-high performance liquid chromatography (UPLC)-MS/MS. Data were analyzed for metabolites differentially abundant in nigericin-treated samples. Dotted lines indicate false discovery rate (FDR) = 0.05 (y axis) and fold change = 2 (x axis). Only metabolites of the indicated groups were highlighted by color that were above these thresholds, except for TCA cycle intermediates (A). Pathway enrichment analysis was performed for suggestive annotations in the KEGG pathway database (FDR < 0.1; number of metabolites in each pathway set ≥2; dotted line indicates the significance threshold of −log₁₀[0.05]). Metabolic pathways are labeled in bold (B).

(legend continued on next page)

although both potently inhibit apoptosis in these cells (Figure 4F). Only in combination with 2-DG were FCCP and nigericin able to reduce cellular ATP in these cells, confirming that they suppress mitochondrial ATP production but that this is compensated.[12] Similarly, other apoptosis-inhibiting ionophores reduced cellular ATP in HCT116 cells only in the presence of 2-DG (Figure S4L). Conversely, although 2-DG alone substantially reduced total cellular ATP in HCT116 cells (Figure 4I), 2-DG treatment did not block apoptosis (Figure S4M). Therefore, depletion of cytoplasmic ATP is not responsible for the ability of uncouplers to inhibit raptinal-induced apoptosis.

Mitochondrial apoptosis is physiologically important during development. In the metamorphosing frog tadpole, multi-ciliated cells are removed from the epidermis by apoptosis upon contact with the developing lateral line during developmental remodeling.[46] We applied FCCP to developing *Xenopus laevis* tadpoles at lateral line migration stages and determined cell death frequency and multi-ciliated cell density. FCCP reduced cell death and increased multi-ciliated cell density (Figures 4J and 4K). These observations suggest that OXPHOS inhibition can interfere with developmental apoptosis in multicellular organisms.

Following the hypothesis that apoptosis inhibition and NLRP3 activation may share a common mechanistic basis, we tested whether the ionophores that could inhibit apoptosis also could activate NLRP3. They all induced NLRP3-dependent IL-1β release and caspase-1 cleavage, demonstrating NLRP3 inflammasome activation (Figures 4L, S4N, and S4O). However, none of the multiple FCCP concentrations tested triggered NLRP3 activation (Figure S4P), although the presence of FCCP shifted the dose-response relationship of nigericin so that lower concentrations become sufficient to trigger the inflammasome (Figure S4Q). This suggests that neither uncoupling nor apoptosis inhibition are sufficient for NLRP3 activation and that other additional effects of the ionophores are required.

Non-ionophore NLRP3 activators and OXPHOS inhibitors suppress apoptosis

We next sought to determine whether non-ionophore NLRP3 activators and inhibitors of the mitochondrial ETC complexes could inhibit apoptosis. We previously found that certain small molecules of the imidazoquinoline family, including imiquimod and CL097, can activate NLRP3 in a K^+ efflux-independent manner by inhibiting complex I of the ETC.[8] They also suppressed raptinal-induced apoptosis at doses that trigger NLRP3

(Figures 5A and S5A). By contrast, the imidazoquinoline resiquimod, which does not engage NLRP3,[8] also did not suppress apoptosis or ATP production (Figures 5A and S5B). We next examined whether other direct inhibitors of ETC complexes could suppress apoptosis. Indeed, rotenone, antimycin A, and potassium cyanide[42] blocked both raptinal-induced cytochrome *c* release from mitochondria and caspase-3 and -9 cleavage (Figures 5B, S5C, and S5D), reminiscent of the observations by Palchaudhuri et al.[23] Similarly, other ETC inhibitors such as piericidin, metformin, or sodium azide prevented apoptosis (Figures S5E–S5G). ETC inhibitors prevent NAD^+ regeneration by complex I, while uncouplers promote it, suggesting that effects on electron transport or NAD^+ are not involved in NLRP3 activation or apoptosis suppression. The F_1F_O ATP synthase (complex V) inhibitor oligomycin[42] also prevented apoptosis and caused significant morphological changes in mitochondria comparable to those observed with uncouplers (Figures 5B, 5C, S5C, and S5H). Dimers of F_1F_O ATP synthase have been suggested to affect cristae membrane curvature and thereby architecture.[29,31,47–50] We analyzed F_1F_O ATP synthase dimer formation and found that both nigericin and oligomycin induced a 3- to 4-fold increase (Figure 5D). As for uncouplers, ETC inhibition reduced mitochondrial ATP production in different cell types, as visualized by targeting an ATP biosensor to the mitochondrial matrix[51] (Figure S5J). Uncouplers and inhibitors of the ETC complexes disrupt the normal mitochondrial proton gradient and thereby their membrane potential and pH, while oligomycin has the opposite effect. The common effects of all these compounds are a reduction of ATP synthase activity and mitochondrial ATP production (see Figure S2E). To determine whether these effects are necessary for their inhibition of apoptosis, we employed two small molecule electron shunts. Pyocyanin and idebenone enable bypassing of complex III or I, respectively, restoring electron transport and ATP production (Figures S5K and S5L).[52,53] They restored the capacity for apoptosis induction in cells treated with inhibitors of complex III and complex I, respectively (Figures 5E, 5F, S5M, and S5N). Similarly, expression of AOX, a protein that can functionally compensate for complex III inhibition in electron transport, restored apoptosis in the presence of antimycin A but not nigericin (Figures 5G and S5O). Collectively, our data support the conclusion that uncouplers, ETC complex inhibitors, and ATP synthase inhibitors suppress apoptosis through inhibition of mitochondrial ATP synthase activity and/or reduction of ATP production or concentrations and disruption of mitochondrial cristae morphology.

(C) After LPS priming and treatment for 1 h, cellular ATP was determined using a luminescent assay and depicted relative to untreated cells. Combined data of three independent experiments are shown.

(D) Principal-component analysis (PCA) for metabolite features of each condition of (A) and (B) was performed.

(E) After treatment for 1.5 h, cytochrome *c* release was assessed by flow cytometry.

(F and G) After treatment for 1.5 h, caspase cleavage was determined as in Figures 1B–1F.

(H) After treatment for 1 h, cytochrome *c* release was quantified as in Figure 3A.

(I) After treatment for 1 h, cellular ATP was determined using a luminescent assay and is depicted in relative light units (RLUs).

(J and K) *Xenopus* embryos were treated with 0.05 μM FCCP (16 h, 16°C, protected from light) at stage 39/40. *Xenopus* stage 41 tadpoles were analyzed by TUNEL staining (J and K) and immunofluorescence imaging for acetylated-α-tubulin to stain cilia (K). The numbers of apoptotic cells in the lateral-line migration paths were quantified. Black boxes in the left images indicate area shown for immunofluorescence.

(L) After LPS priming and treatment for 4 h, IL-1β was quantified by ELISA.

For statistical analysis, paired (C) and unpaired (I and J) t tests were performed. Data are depicted as mean ±SD (C, I, J, and L) and are representative of two (E, H, J, and K) or at least three independent experiments (F, G, I, and L). See also Figure S4.

Significance levels are denoted as *$p < 0.05$, **$p < 0.01$, ***$p < 0.001$, and ns for not significant.
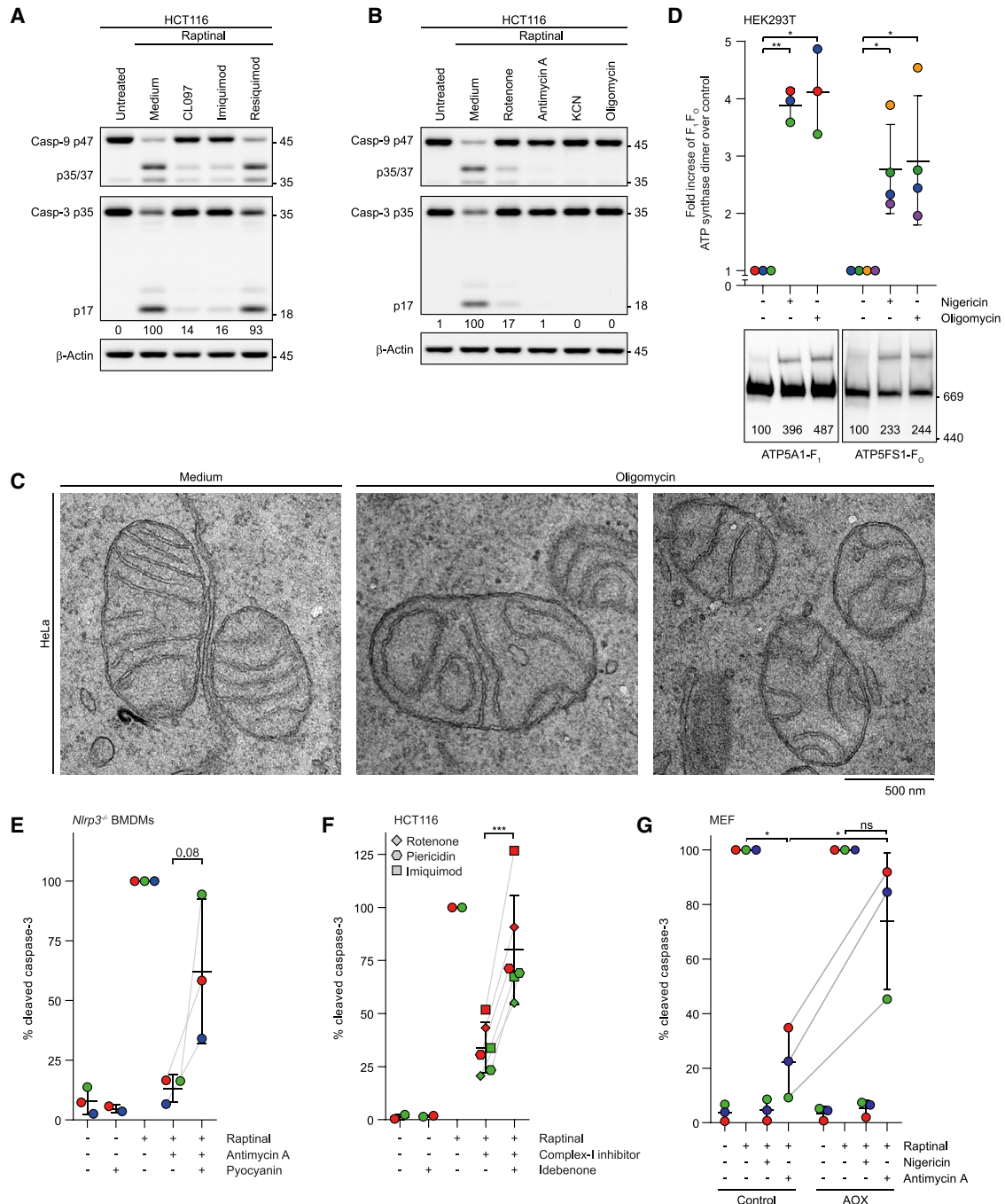
Figure 5. Imidazoquinolines and other ETC and OXPHOS inhibitors suppress apoptosis

(A–G) Indicated human (A–D and F) or murine wild-type or inflammasome-deficient (E and G) cell types were treated as indicated.

(A and B) After treatment for 2 h, caspase cleavage was quantified as in Figures 1B–1F.

(C) After treatment for 0.5 h, mitochondrial morphology was assessed by TEM.

(D) Isolated mitochondria were treated for 12 h, and F_1F_O ATP synthase monomers and dimers were determined by blue native PAGE and immunoblotting. Signals were quantified, and the fold increase of dimer over control after treatment was calculated for three (F_1) or four (F_O) independent experiments (top) of which one is shown (bottom). Colors depict data points from the same replicate.

(E and F) Cells were LPS-primed (E), pre-treated with pyocyanin (E) or idebenone (F) for 0.5 h, and stimulated for 1.5 h. Caspase cleavage was quantified and is depicted relative to cells treated with raptinal only. Pooled data of three (E) or two (F) independent experiments are depicted of which one is shown in Figures S5M or S5N, respectively. Colors depict data points from the same replicate.

Physiological NLRP3 activators suppress apoptosis

Our data suggest a strong overlap between the factors that can inhibit apoptosis and those that activate NLRP3. We asked whether these properties were shared by physiological activators of NLRP3. Extracellular ATP is an endogenous NLRP3 activator generated during conditions of tissue damage. ATP activates the purinergic receptor channel P2X$_7$, triggering K$^+$ efflux and NLRP3 activation.[54] We found that ATP-induced NLRP3 inflammasome activation prevailed when raptinal was added simultaneously, and ATP also suppressed raptinal-induced caspase-3 cleavage in a P2X$_7$-dependent but inflammasome-independent manner (Figures 6A, 6B, and S6A). If and how extracellular ATP can influence mitochondrial function is unclear, and we analyzed its metabolic effects. Untargeted metabolomics showed that extracellular ATP also caused substantial metabolic changes with a strong overlap to the effects of nigericin (Figures 6C, 6D, and S6B). ATP additionally caused a drop in TCA cycle intermediates and the accumulation of components of glycolysis (Figures 4A and 6C). Extracellular flux analysis confirmed strongly and rapidly increased glycolysis upon ATP treatment (Figure 6E). This suggests that extracellular ATP-induced P2X$_7$ signaling not only activates NLRP3 but also disrupts mitochondrial processes, including core metabolism and apoptosis induction.

Endogenous and exogenous particulate activators such as gout-associated MSU crystals or the adjuvant alum trigger NLRP3 by causing lysosomal destabilization. Consistent with a recent report showing that lysosomal proteases attack mitochondrial ETC components when released to the cytoplasm upon lysosomal damage,[55] MSU and alum also interfered with raptinal-induced apoptosis in macrophages (Figures 6F and S6C).

We postulated that a physiological function of NLRP3 in myeloid cells located throughout the body is to serve as a sensor for factors within the tissue, such as viruses, which attempt to suppress apoptosis. Various viruses directly impact mitochondrial respiration with consequences such as reactive oxygen species (ROS) production and increased glycolysis, but whether this is connected to NLRP3 activation or suppression of apoptosis is unknown.[56] SARS-CoV-2 enters myeloid cells and activates NLRP3 by poorly understood mechanisms.[57–59] It also induces loss of the mitochondrial membrane potential and changes in mitochondrial ultrastructure reminiscent of those we observe with NLRP3 activators and OXPHOS inhibitors.[60] SARS-CoV-2 infection strongly suppressed raptinal-induced caspase-3 cleavage *in vitro* (Figures 6G and S6D). Similarly, modified vaccinia Ankara (MVA) virus[61] also inhibited raptinal-induced apoptosis (Figure 6H). To test whether the ability to inhibit apoptosis and to trigger NLRP3 are mechanistically connected, we turned to a third virus, influenza A. We confirmed that inflammasome activation by influenza depends on a fully functional NS1 virulence factor. While wild-type H1N1 caused inflammasome activation, a virus carrying a truncated version of NS1

(H1N1-ΔNS1), although replicating normally, failed to trigger caspase-1 and IL-1β cleavage and release (Figure S6E). Similar to SARS-CoV-2 and MVA, wild-type H1N1 was able to suppress raptinal-induced caspase-3 cleavage, while a ΔNS1-carrying virus also failed to inhibit apoptosis (Figures 6I, S6F, and S6G). Thus, physiological and disease-relevant activators of NLRP3 inhibit BAX/BAK-independent mitochondrial apoptosis triggered by raptinal.

Inhibitors of mitochondrial ATP production can trigger NLRP3 in the presence of a second signal

Although our data showed a correlation between the abilities to inhibit apoptosis and to activate NLRP3, conventional OXPHOS inhibitors that all suppressed apoptosis failed to activate NLRP3 (Figures 7A and 7B). Thus, we conclude that neither inhibition of mitochondrial ATP production nor suppression of apoptosis was sufficient for NLRP3 activation. This is in line with our previous work and subsequent studies by others suggesting that complex I inhibition by imiquimod is necessary but not sufficient for NLRP3 activation by this imidazoquinoline and that additional effects of imidazoquinolines might contribute to NLRP3 activation.[8,10] We tested whether OXPHOS inhibitors can acquire the ability to activate NLRP3 when an additional stimulus was provided, using the imidazoquinolines resiquimod or gardiquimod that do not trigger NLRP3.[8] Indeed, the different OXPHOS inhibitors induced robust NLRP3-dependent inflammasome activation only when combined with an imidazoquinoline (Figures 7A, 7B, and S7A–S7C). We next asked whether intact electron transport and mitochondrial ATP synthesis are required for NLRP3 activation by these combinations and again employed the electron shunt pyocyanin.[53] NLRP3 activation by the complex III inhibitor antimycin A + resiquimod was blocked by pyocyanin, whereas NLRP3 activation by the uncoupler FCCP + resiquimod remained intact (Figures 7C, 7D, and S7E). These data suggest that suppression of mitochondrial ATP production by ETC inhibitors (and not altered ETC activity itself) provides a signal that is essential for NLRP3 activation elicited by ETC inhibitors.

NLRP3 activators, including imiquimod and CL097, have previously been reported to induce clustering and recruitment of NLRP3 to cellular vesicles of Golgi apparatus or endosomal origin.[17–19,62] Similarly, resiquimod alone induced formation of NLRP3 aggregates (also called speckles) colocalizing with vesicles positive for TGN46, while ETC inhibitors did not (Figures 7D, 7E, and S7F). Therefore, the ability of resiquimod to provide the second signal for NLRP3 activation might reside in its ability to induce NLRP3 aggregation and vesicle recruitment.

Since inhibition of apoptosis by K$^+$ efflux-dependent NLRP3 activators did not rely on K$^+$ efflux (Figures 3B and S3C), and since neither non-NLRP3 activating OXPHOS (and apoptosis) inhibitors nor imidazoquinolines do generally cause K$^+$ efflux[8] (Figure S7G), we speculated that the role of K$^+$ efflux might reside in the non-mitochondrial, vesicular signal for NLRP3 activation, as also previously hypothesized.[16–18] Signaling by the

---

(G) AOX-expressing or empty vector control MEFs were treated for 1–2 h. Caspase cleavage was quantified as in Figures 1B–1F. Pooled data from three biological replicates are depicted of which one is shown in Figure S5O. Colors depict data points from the same replicate.

For statistical analysis, paired t tests were performed (D–G). Data are depicted as mean ±SD (D–G) and representative of at least three independent experiments (A and B). See also Figure S5.

Significance levels are denoted as *p < 0.05, **p < 0.01, ***p < 0.001, and ns for not significant.
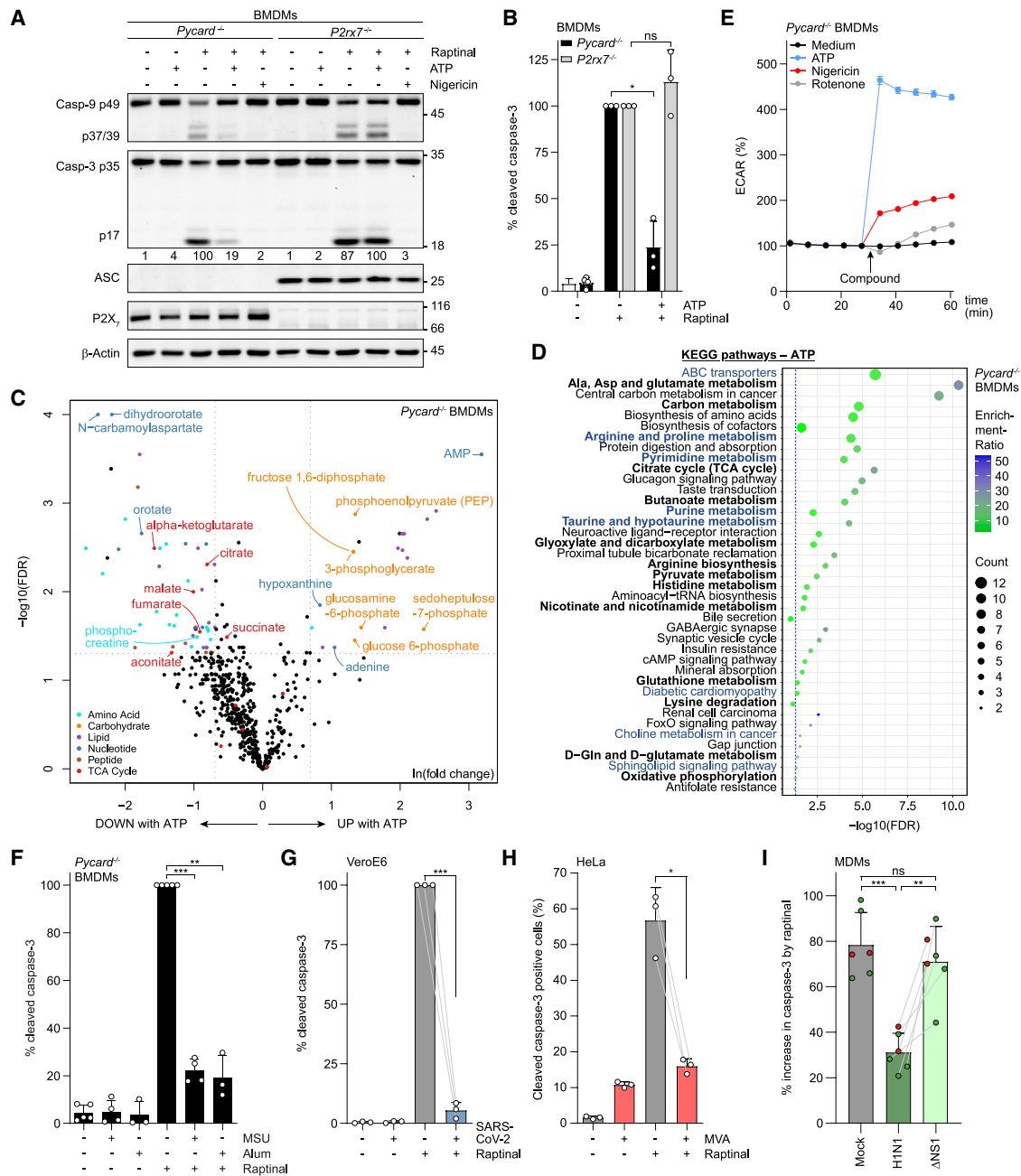
Figure 6. Physiological NLRP3 activators suppress apoptosis

(A–I) Indicated murine gene-deficient (A–F), simian (G), or human (H and I) cell types were treated as indicated.

(A and B) After LPS priming and treatment for 1.5 h, caspase cleavage was determined as in Figures 1F (A). Combined data of three independent experiments are shown (B).

(C and D) After LPS priming and treatment for 1 h, metabolites were extracted and measured by UPLC-MS/MS. Data were analyzed for metabolites differentially abundant in ATP-treated samples. Dotted lines indicate false discovery rate (FDR) = 0.05 (y axis) and fold change = 2 (x axis). Only metabolites of the indicated groups were highlighted by color that were above these thresholds, except for TCA cycle intermediates (C). Pathway enrichment analysis was performed for suggestive annotations in the KEGG pathway database (FDR < 0.1; number of metabolites in each pathway set ≥ 2; dotted line indicates the significance threshold of $-\log_{10}[0.05]$). Metabolic pathways are labeled in bold. Hits that were also detected for nigericin (Figure 4B) are in blue (D).

(E) Before and after treatment, extracellular acidification rate (ECAR) was measured.

(F) After treatment for 2 h, caspase cleavage was determined as in Figures 1B–1F. Pooled data from three (alum) or four (MSU) independent experiments are depicted of which one is shown in Figure S6C.

(G) After SARS-CoV-2 (B.1.1.7, MOI = 1) infection for 16 h and treatment with 20 μM raptinal for 1.5 h, caspase cleavage was quantified as in Figures 1B–1F. Pooled data of three independent experiments are depicted of which one is shown in Figure S6D.

mechanoreceptor ion channel Piezo-1 such as induced by its pharmacological activator Yoda-1 alone cannot cause but boosts NLRP3 activation in the presence of suboptimal concentration of NLRP3 activators, which was connected to KCNN4 activation and K^{+} efflux.[63] These results are reminiscent of our observation that OXPHOS inhibitors of any mode-of-action shift the dose-response relationship of nigericin so that less is sufficient for NLRP3 activation (Figures S4Q and S7H). We therefore tested the combination of Piezo-1 activation and OXPHOS inhibition for inflammasome activation. Although Yoda-1 or oligomycin alone were unable to do so, their combination triggered robust, NLRP3-dependent IL-1β release (Figures 7F–7H and S7I). Together, these data suggest that in addition to imidazoquinolines, activity of the ion channel Piezo-1 can provide a second signal that, together with OXPHOS inhibition, is sufficient to trigger NLRP3.

DISCUSSION

Here, we have shown that suppression of mitochondrial apoptosis is a pervasive property of structurally diverse NLRP3 activators. Suppression of apoptosis was not a result of NLRP3 activation since apoptosis inhibition was intact in non-inflammasome-competent cells. Mechanistically, NLRP3 activators suppressed mitochondrial ATP production. This led to increased F_1F_O ATP synthase dimerization, disturbed mitochondrial morphology with cristae rearrangements and closure of crista junctions, and the inhibition of cytochrome c release. Although our data suggest a strong overlap between factors that inhibit OXPHOS and apoptosis and those that can activate NLRP3, and although suppression of OXPHOS was required both for apoptosis inhibition and NLRP3 activation, it was not sufficient for triggering NLRP3, which required a second signal. This is in line with a large body of literature suggesting multiple signals are involved in NLRP3 activation.[6,7]

Our results are consistent with a model in which NLRP3 activators and OXPHOS inhibitors promote cristae rearrangements with closure of crista junctions or fission of cristae from the inner boundary membrane, thereby trapping cytochrome c in the cristae lumen. Aside from OPA1 and the MICOS complex,[31,37,38] dimers of F_1F_O ATP synthase have also been implicated in establishment and maintenance of cristae architecture.[29,31,47–50] Our results imply that the aberrations in mitochondrial morphology that lead to trapping of cytochrome c are a result of reduced mitochondrial ATP production or amounts. Decreased mitochondrial ATP concentrations might themselves result in changes to mitochondrial morphology. Alternatively, it is tempting to speculate that ETC inhibitors and uncouplers might cause apoptosis-precluding changes in cristae morphology by affecting the structural functions of F_1F_O ATP synthase. Further-

more, in addition to structural changes, increased binding to cardiolipin and complex III and IV might contribute to cytochrome c being unavailable for apoptosis under conditions of OXPHOS inhibition. Further studies will be needed to address these hypotheses and to elucidate a potential beneficial physiological function of mitochondrial apoptosis prevention under conditions of OXPHOS inhibition independent of inflammasome activation.

The pervasive ability of structurally diverse NLRP3 activators to disrupt mitochondria and suppress apoptosis is suggestive of a general role for mitochondria in NLRP3 activation, as it has been implicated by many studies for specific activators.[6–8,10,11,64] We observed that classical inhibitors of OXPHOS are not sufficient for NLRP3 activation. Nonetheless, the data presented here as well as that of our previous study[8] suggest that substances that disrupt mitochondrial ATP production do indeed provide signals for NLRP3 activation. We postulate that mitochondrial signals are not sufficient but are universally required for NLRP3 activation. This concept is supported by our finding that diverse NLRP3 activators that are not recognized as direct OXPHOS inhibitors nonetheless impair mitochondrial ATP production, disrupt mitochondrial morphology, or block apoptosis, as well as by various reports of mitochondrial effects of nigericin and extracellular ATP and of lysosomal damage as induced by MSU or alum and viruses including SARS-CoV-2.[40,56,60,65,66]

We found that classical OXPHOS inhibitors acquired the ability to robustly activate NLRP3 when combined with resiquimod or gardiquimod. Since these imidazoquinolines alone failed to activate NLRP3, the data suggest that they provide an additional signal that—similar to the mitochondrial signal—is also necessary but not sufficient for NLRP3 activation. The nature of this signal remains unclear. However, given the ability of imidazoquinolines to activate TLR7 and/or TLR8 on the endosome and the recent implication of the endosomal compartment and the *trans*-Golgi network in NLRP3 activation,[16–19] it is possible that this compartment provides the additional signal. Our observation that resiquimod causes NLRP3 aggregate (speckle) formation and vesicle recruitment—while classical OXPHOS inhibitors do not—indeed points in this direction.

We therefore propose a "two activation signals" model for NLRP3 activation in which the mitochondrial signal and an additional signal are both simultaneously required but alone not sufficient for NLRP3 activation. Two-signal activation modes are widespread as safeguard mechanisms in many biological processes, including activation of immune cells and their receptors.[67] Of note, we refer to this as a "two activation signals model" to distinguish from the established "two-signal model" for NLRP3 activation that is already well accepted in the field. In the latter, the two "signals" were defined as the exogenous factors that (1) upregulate NLRP3 expression (1a) and cause

---

(H) After MVA infection (MOI = 2) for 14.5 h and treatment with 20 μM raptinal for 1.5 h, caspase-3 cleavage was determined by flow cytometry. Pooled data of three biological replicates are depicted.

(I) After infection with influenza A virus (H1N1) or H1N1-ΔNS1 (ΔNS1) (MOI = 1, 12 h [green], or MOI = 10, 9 h [red]), cells were treated with 5-μM raptinal for 2 h. Caspase-3 cleavage was determined by immunoblotting. The increase in caspase-3 cleavage by raptinal treatment is depicted per infection condition from 6 biological replicates. Raw data are shown in Figures S6F and S6G.

For statistical analysis, paired t tests were performed (B and F–I). Data are depicted as mean ± SD (B and F–I) or ± SEM (E) and are representative of three independent experiments (A and E). See also Figure S6.

Significance levels are denoted as *$p < 0.05$, **$p < 0.01$, ***$p < 0.001$, and ns for not significant.
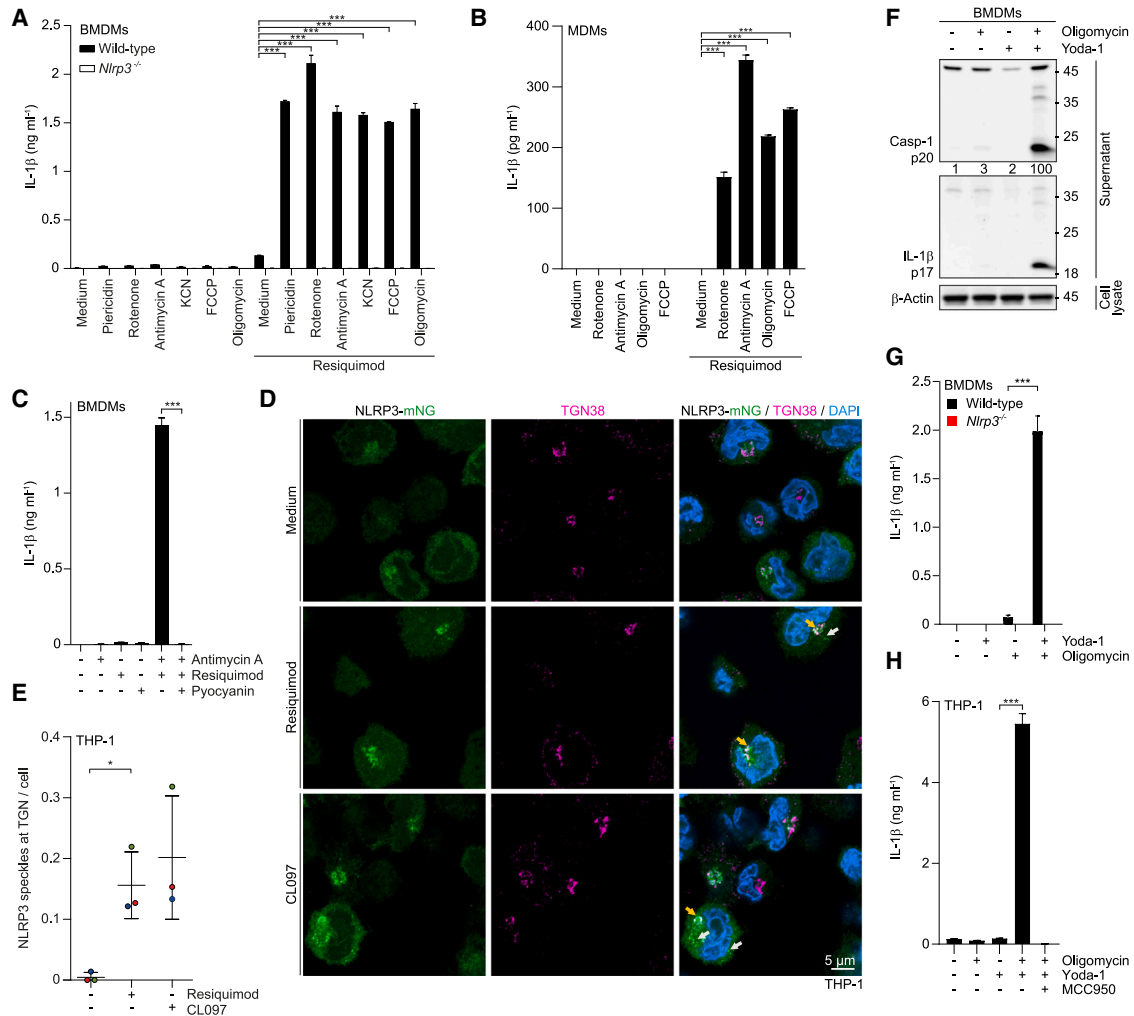
Figure 7. Inhibitors of mitochondrial ATP production can trigger NLRP3 in the presence of a second signal

(A–H) Indicated murine (A, C, F, and G) or human (B, D, E, and H) wild-type or inflammasome-deficient cell types were treated as indicated.

(A and B) After LPS priming and treatment in the presence or absence of 300 (A) or 400 μM (B) resiquimod for 3 h, IL-1β was quantified by ELISA.

(C) After LPS priming and pre-treatment with pyocyanin for 0.5 h, cells were treated for 3 h, and IL-1β was quantified by ELISA.

(D and E) $NLRP3^{-/-}$ THP-1 cells reconstituted with NLRP3 WT-mNG were treated for 1 h. NLRP3 localization and speckle formation at the TGN was assessed by confocal fluorescence microscopy. White and orange arrows denote speckles located outside or in the TGN, respectively (D). Speckles located at the TGN were quantified and depicted as ration of speckles in the TGN per nuclei. Pooled data from three replicates are depicted (E).

(F–H) After LPS priming and treatment for 2 h (H) or 3 h (F and G), protein cleavage was determined as in Figure 1B (F) and IL-1β release by ELISA (G and H). For statistical analysis, METs (A–C, G, and H) and a paired t test (E) were performed. Data are depicted as mean ± SD (A–C, E, G, and H) and are representative of two (B) or at least three independent experiments (A, C, D, and F–H). See also Figure S7.

Significance levels are denoted as $^*p < 0.05$, $^{**}p < 0.01$, $^{***}p < 0.001$, and ns for not significant.

---

changes in post-translational modifications (1b) not sufficient of activation (i.e., the "priming" signal[20]), and (2) trigger actual NLRP3 activation (the individual experimental activators of NLRP3, e.g., nigericin, extracellular ATP, imiquimod, particulates destabilizing the lysosome and causing membrane damage, K^+ efflux,[68] etc.). By contrast, our model refers to the intracellular signals required for the conversion of primed NLRP3 from the inactive to the active state. This model would suggest that imiquimod and CL097 can activate NLRP3 because they provide the mitochondrial signal (2a) and the additional signal (2b) simultaneously. Furthermore, the model would predict that other NLRP3 activators such as nigericin (and other H^+/K^+ iono-

phores), extracellular ATP, particles, and viruses also provide the additional (potentially endosomal) signal. Consistent with this hypothesis, several of these activators have been shown to induce binding of NLRP3 to PI(4)P at TGN46-positive cellular vesicles.[16–18] However, whether NLRP3 speckle formation[19,62] and TGN46 recruitment are similarly pervasive abilities of NLRP3 activators required for activation will have to be studied by future research. An open question is how K^+ efflux, which is implicated in NLRP3 activation by some (e.g., nigericin, ATP) but not all (e.g., imidazoquinolines) triggers, factors into this model. Our observation that activation of the Piezo-1 ion channel can trigger NLRP3 when combined with F_1F_O ATP synthase inhibition

suggests that a combination of mechanical and metabolic stress might be sufficient to trigger NLRP3. Such a combination of stresses might occur during viral infection but could also be connected to sterile conditions with NLRP3-mediated pathology such as gout or (e.g., cardiac) ischemia. Further research will be required to elucidate this.

NLRP3 does not sense pathogens directly but instead responds to (a combination of) cellular stress signals.[6,7] Our study has shown that apoptosis inhibition is a widespread feature of NLRP3 activators. NLRP3 does not seem to sense inhibition of apoptosis directly; instead, suppression of mitochondrial ATP production simultaneously inhibits apoptosis and provides a signal for NLRP3 activation. Many intracellular pathogens, in particular viruses, have developed strategies to inhibit apoptosis of host cells,[56] and inducing intrinsic apoptosis using BH3-mimetic drugs in viral and bacterial infections can be therapeutically beneficial,[69,70] collectively suggesting that apoptosis can serve as a host defense mechanism. Thus, our results support the hypothesis that NLRP3 may have evolved as a guard sensor involved in defense against pathogens that can at least partially overcome direct sensing by other innate immune receptors and other host defense mechanisms, including apoptosis.

Apoptosis and regulated cell lysis (e.g., pyroptosis and necroptosis) are fundamentally distinct in their mechanisms and physiological functions. Appropriate cellular decision-making between these cell death modalities has far-reaching consequences for the surrounding tissue in achieving a balance between robust, protective immunity and avoiding tissue damage to maintain tissue homeostasis. Recent work has shown that cellular switches provide stringent control over these cell death pathways. Caspase-8, for instance, acts as a switch between apoptosis, necroptosis, and pyroptosis. In its enzymatically active form, it drives apoptosis and suppresses necroptosis, and its inactivation or absence results in activation of RIPK3 and MLKL, executing necroptosis, and can also trigger ASC-caspase-1 and caspase-11 signaling.[71,72] Notably, caspase-8 also has the capacity to activate pyroptosis via the inflammasome.[73,74] Apoptosis is accompanied by early degradation of pro-IL-1β and GSDMD,[26] and the apoptotic effector caspase-7 can counteract inflammasome-driven pyroptosis by promoting membrane repair.[75] In previous work, we demonstrated that caspase-1 enzymatic activity acts as a switch between GSDMD-driven pyroptosis and caspase-8-driven non-canonical pyroptosis.[76] In this study, we show that mitochondria are central to early-stage decision-making between apoptosis and NLRP3-driven pyroptosis (before caspase-1 and caspase-3 activation). Our data suggest that acute inhibition of mitochondrial ATP production not only provides a signal for NLRP3 activation but simultaneously suppresses apoptosis, thus acting as a switch between these two cell death pathways. We propose that this represents a mechanism to ensuring stringency in cell death decisions.

Limitations of the study

Several limitations such as the unknown nature of the second (non-mitochondrial) NLRP3 activating signal, the unclear contribution of NLRP3 binding to PI(4)P at TGN46-positive cellular vesicles, the elusive role of K$^+$ efflux, and the necessity to further elucidate the precise mechanisms preventing cytochrome *c* release upon OXPHOS inhibition were already discussed above. An additional key open question is how NLRP3 in the cytoplasm senses mitochondrial perturbations caused by OXPHOS inhibitors. Previous studies, including our own work, have suggested mitochondrial ROS, release of oxidized mitochondrial DNA, and exposure of the inner mitochondrial membrane lipid cardiolipin on the outer membrane as mitochondrial signals for NLRP3 activation.[6–9,77] These events were independently also attributed to OXPHOS inhibitors, such as for cardiolipin that is externalized to the outer mitochondrial membrane when cells are treated with rotenone or FCCP.[78] Further studies will be needed not only to determine the precise nature of the "mitochondrial" signal(s) activating NLRP3 but also whether the signal arises from a drop in ATP synthase activity, a reduction in mitochondrial ATP concentrations, or morphological changes in mitochondria. Finally, verifying the *in vivo* impact of blocked OXPHOS on apoptosis and NLRP3 activation and thereby on development, homeostasis, and immunity was difficult to ascertain in this work due to the toxicity of OXPHOS inhibition in mammals.

AUTHOR CONTRIBUTIONS

B.S.S., S.W., L.F., C.D., I.L.I., S. Kessler, M.M.-T., O. Gorka, F.L., E.N., G.W., A.M., C. Koentges, C.U., P.A., P.R., S.G., S. Kirschnek, C. Meisinger, J.P., H.F.-M., A.O., V.G.D., F.S., J.A.Z., A.C., D.W., K.S.B., Y.-H.T., K.N., and M.H. performed experiments and analyzed data. Y.C. performed bioinformatics analyses with support by J.B. C. Kreutz and Y.C. performed statistical analyses. B.S.S. prepared figures and wrote figure legends and the STAR Methods section of the manuscript with input from other authors. Y.-H.T., T.M., and M.K. contributed to in vitro imaging experiments. D.R. performed transmission electron microscopy for 3D tomography. O. Gorka, K.C., T.M., M.K., R.B., P.W., U.M., A.S.R., J.E.V., F.E., R.M., M.R., R.P., G.H., K.K., C. Meisinger, T.H., A.K., S.J., A.N.R.W., and M.S. supervised a portion of the work. O. Groß and C.J.G. wrote the main text of the manuscript, with the help of B.S.S. O. Groß conceived and oversaw the project.

DECLARATION OF INTERESTS

E.N. and O. Groß are coinventors on patent applications for immunomodulators and co-founders of EMUNO Therapeutics, a company developing drugs that control immunity to address unmet clinical needs. None of the drug candidates in patenting or development were used in this study.

STAR★METHODS

Detailed methods are provided in the online version of this paper and include the following:

- KEY RESOURCES TABLE
- EXPERIMENTAL MODEL AND STUDY PARTICIPANT DETAILS
  - Mice
  - BMDM and BMDC preparation
  - Cell lines
  - Preparation of PBMCs and MDMs
  - Preparation of primary thymocytes
  - Preparation of microglia
  - Preparation of Kupffer cell
  - Xenopus animal culture
- METHOD DETAILS
  - Inflammasome stimulation
  - Apoptosis induction and co-stimulation
  - Viral infection
  - Immunodetection of proteins
  - Cell viability assays
  - Cell death characterization by flow cytometry
  - Incucyte live cell imaging
  - MOMP in isolated mitochondria
  - Cytochrome c release assay
  - Digitonin-mediated MOMP
  - Blue Native PAGE of isolated mitochondria
  - Brightfield imaging
  - Immunofluorescence and confocal imaging
  - Transmission electron microscopy
  - Classification of mitochondrial ultrastructure
  - Measurement of cellular potassium levels
  - Subcellular ATP measurements
  - Metabolic analysis
  - Metabolomics
  - Xenopus animal experiments
- QUANTIFICATION AND STATISTICAL ANALYSIS
  - Statistical analysis
  - Replicates and data depiction
  - Quantifications

SUPPLEMENTAL INFORMATION

Supplemental information can be found online at https://doi.org/10.1016/j.immuni.2024.10.012.

REFERENCES

1. Martinon, F., Burns, K., and Tschopp, J. (2002). The inflammasome: A molecular platform triggering activation of inflammatory caspases and processing of proIL-β. Mol. Cell 10, 417–426. https://doi.org/10.1016/S1097-2765(02)00599-3.

2. Fernandes-Alnemri, T., Wu, J., Yu, J.W., Datta, P., Miller, B., Jankowski, W., Rosenberg, S., Zhang, J., and Alnemri, E.S. (2007). The pyroptosome: a supramolecular assembly of ASC dimers mediating inflammatory cell death via caspase-1 activation. Cell Death Differ. 14, 1590–1604. https://doi.org/10.1038/sj.cdd.4402194.

3. Shi, J., Zhao, Y., Wang, K., Shi, X., Wang, Y., Huang, H., Zhuang, Y., Cai, T., Wang, F., and Shao, F. (2015). Cleavage of GSDMD by inflammatory caspases determines pyroptotic cell death. Nature 526, 660–665. https://doi.org/10.1038/NATURE15514.

4. Guo, H., Callaway, J.B., and Ting, J.P.Y. (2015). Inflammasomes: mechanism of action, role in disease, and therapeutics. Nat. Med. 21, 677–687. https://doi.org/10.1038/nm.3893.

5. Coll, R.C., O'Neill, L., and Schroder, K. (2016). Questions and controversies in innate immune research: what is the physiological role of NLRP3? Cell Death Discov. 2, 16019. https://doi.org/10.1038/cddiscovery.2016.19.

6. Akbal, A., Dernst, A., Lovotti, M., Mangan, M.S.J., McManus, R.M., and Latz, E. (2022). How location and cellular signaling combine to activate the NLRP3 inflammasome. Cell. Mol. Immunol. 19, 1201–1214. https://doi.org/10.1038/s41423-022-00922-w.

7. Neuwirt, E., Gorka, O., Saller, B.S., Groß, C.J., Madl, T., and Groß, O. (2021). NLRP3 as a sensor of metabolism gone awry. Curr. Opin. Biotechnol. 68, 300–309. https://doi.org/10.1016/J.COPBIO.2021.03.009.

8. Groß, C.J., Mishra, R., Schneider, K.S., Médard, G., Wettmarshausen, J., Dittlein, D.C., Shi, H., Gorka, O., Koenig, P.A., Fromm, S., et al. (2016). K+ efflux-independent NLRP3 inflammasome activation by small molecules targeting mitochondria. Immunity 45, 761–773. https://doi.org/10.1016/J.IMMUNI.2016.08.010.

9. Iyer, S.S., He, Q., Janczy, J.R., Elliott, E.I., Zhong, Z., Olivier, A.K., Sadler, J.J., Knepper-Adrian, V., Han, R., Qiao, L., et al. (2013). Mitochondrial cardiolipin is required for Nlrp3 inflammasome activation. Immunity 39, 311–323. https://doi.org/10.1016/J.IMMUNI.2013.08.001.

10. Billingham, L.K., Stoolman, J.S., Vasan, K., Rodriguez, A.E., Poor, T.A., Szibor, M., Jacobs, H.T., Reczek, C.R., Rashidi, A., Zhang, P., et al. (2022). Mitochondrial electron transport chain is necessary for NLRP3 inflammasome activation. Nat. Immunol. 23, 692–704. https://doi.org/10.1038/s41590-022-01185-3.

11. Zhou, R., Yazdi, A.S., Menu, P., and Tschopp, J. (2011). A role for mitochondria in NLRP3 inflammasome activation. Nature 469, 221–225. https://doi.org/10.1038/NATURE09663.

12. Muñoz-Planillo, R., Kuffa, P., Martínez-Colón, G., Smith, B.L., Rajendiran, T.M., and Núñez, G. (2013). K+ efflux is the common trigger of NLRP3

inflammasome activation by bacterial toxins and particulate matter. Immunity 38, 1142–1153. https://doi.org/10.1016/j.immuni.2013.05.016.

13. Gaidt, M.M., Ebert, T.S., Chauhan, D., Schmidt, T., Schmid-Burgk, J.L., Rapino, F., Robertson, A.A.B., Cooper, M.A., Graf, T., and Hornung, V. (2016). Human monocytes engage an alternative inflammasome pathway. Immunity 44, 833–846. https://doi.org/10.1016/J.IMMUNI.2016.01.012.

14. Wolf, A.J., Reyes, C.N., Liang, W., Becker, C., Shimada, K., Wheeler, M.L., Cho, H.C., Popescu, N.I., Coggeshall, K.M., Arditi, M., et al. (2016). Hexokinase is an innate immune receptor for the detection of bacterial peptidoglycan. Cell 166, 624–636. https://doi.org/10.1016/J.CELL.2016.05.076.

15. Tapia-Abellán, A., Angosto-Bazarra, D., Alarcón-Vila, C., Baños, M.C., Hafner-Bratkovič, I., Oliva, B., and Pelegrín, P. (2021). Sensing low intracellular potassium by NLRP3 results in a stable open structure that promotes inflammasome activation. Sci. Adv. 7, 4468–4483. https://doi.org/10.1126/sciadv.abf4468.

16. Andreeva, L., David, L., Rawson, S., Shen, C., Pasricha, T., Pelegrin, P., and Wu, H. (2021). NLRP3 cages revealed by full-length mouse NLRP3 structure control pathway activation. Cell 184, 6299–6312.e22. https://doi.org/10.1016/j.cell.2021.11.011.

17. Zhang, Z., Venditti, R., Ran, L., Liu, Z., Vivot, K., Schürmann, A., Bonifacino, J.S., De Matteis, M.A., and Ricci, R. (2023). Distinct changes in endosomal composition promote NLRP3 inflammasome activation. Nat. Immunol. 24, 30–41. https://doi.org/10.1038/S41590-022-01355-3.

18. Chen, J., and Chen, Z.J. (2018). PtdIns4P on dispersed trans-Golgi network mediates NLRP3 inflammasome activation. Nature 7734, 71–76. https://doi.org/10.1038/s41586-018-0761-3.

19. Magupalli, V.G., Negro, R., Tian, Y., Hauenstein, A.V., Di Caprio, G., Skillern, W., Deng, Q., Orning, P., Alam, H.B., Maliga, Z., et al. (2020). HDAC6 mediates an aggresome-like mechanism for NLRP3 and pyrin inflammasome activation. Science 369, eaas8995. https://doi.org/10.1126/SCIENCE.AAS8995.

20. Bauernfeind, F.G., Horvath, G., Stutz, A., Alnemri, E.S., MacDonald, K., Speert, D., Fernandes-Alnemri, T., Wu, J., Monks, B.G., Fitzgerald, K.A., et al. (2009). Cutting edge: NF-kappaB activating pattern recognition and cytokine receptors license NLRP3 inflammasome activation by regulating NLRP3 expression. J. Immunol. 183, 787–791. https://doi.org/10.4049/JIMMUNOL.0901363.

21. Galluzzi, L., Vitale, I., Aaronson, S.A., Abrams, J.M., Adam, D., Agostinis, P., Alnemri, E.S., Altucci, L., Amelio, I., Andrews, D.W., et al. (2018). Molecular mechanisms of cell death: recommendations of the Nomenclature Committee on Cell Death 2018. Cell Death Differ. 25, 486–541. https://doi.org/10.1038/s41418-017-0012-4.

22. Bock, F.J., and Tait, S.W.G. (2019). Mitochondria as multifaceted regulators of cell death. Nat. Rev. Mol. Cell Biol. 21, 85–100. https://doi.org/10.1038/s41580-019-0173-8.

23. Palchaudhuri, R., Lambrecht, M.J., Botham, R.C., Partlow, K.C., van Ham, T.J., Putt, K.S., Nguyen, L.T., Kim, S.H., Peterson, R.T., Fan, T.M., et al. (2015). A small molecule that induces intrinsic pathway apoptosis with unparalleled speed. Cell Rep. 13, 2027–2036. https://doi.org/10.1016/j.celrep.2015.10.042.

24. Mariathasan, S., Weiss, D.S., Newton, K., McBride, J., O'Rourke, K., Roose-Girma, M., Lee, W.P., Weinrauch, Y., Monack, D.M., and Dixit, V.M. (2006). Cryopyrin activates the inflammasome in response to toxins and ATP. Nature 440, 228–232. https://doi.org/10.1038/nature04515.

25. Miao, E.A., Rajan, J.V., and Aderem, A. (2011). Caspase-1-induced pyroptotic cell death. Immunol. Rev. 243, 206–214. https://doi.org/10.1111/J.1600-065X.2011.01044.X.

26. Taabazuing, C.Y., Okondo, M.C., and Bachovchin, D.A. (2017). Pyroptosis and apoptosis pathways engage in bidirectional crosstalk in monocytes and macrophages. Cell Chem. Biol. 24, 507–514.e4. https://doi.org/10.1016/j.chembiol.2017.03.009.

27. Santavanond, J.P., Chiu, Y.H., Tixeira, R., Liu, Z., Yap, J.K.Y., Chen, K.W., Li, C.L., Lu, Y.R., Roncero-Carol, J., Hoijman, E., et al. (2024). The small molecule raptinal can simultaneously induce apoptosis and inhibit PANX1 activity. Cell Death Dis. 15, 123. https://doi.org/10.1038/S41419-024-06513-Z.

28. Heimer, S., Knoll, G., Schulze-Osthoff, K., and Ehrenschwender, M. (2019). Raptinal bypasses BAX, BAK, and BOK for mitochondrial outer membrane permeabilization and intrinsic apoptosis. Cell Death Dis. 10, 556. https://doi.org/10.1038/s41419-019-1790-z.

29. Quintana-Cabrera, R., Quirin, C., Glytsou, C., Corrado, M., Urbani, A., Pellattiero, A., Calvo, E., Vázquez, J., Enríquez, J.A., Gerle, C., et al. (2018). The cristae modulator optic atrophy 1 requires mitochondrial ATP synthase oligomers to safeguard mitochondrial function. Nat. Commun. 9, 3399. https://doi.org/10.1038/s41467-018-05655-x.

30. Uren, R.T., Dewson, G., Bonzon, C., Lithgow, T., Newmeyer, D.D., and Kluck, R.M. (2005). Mitochondrial release of pro-apoptotic proteins: electrostatic interactions can hold cytochrome c but not Smac/Diablo to mitochondrial membranes. J. Biol. Chem. 280, 2266–2274. https://doi.org/10.1074/JBC.M411106200.

31. Stephan, T., Brüser, C., Deckers, M., Steyer, A.M., Balzarotti, F., Barbot, M., Behr, T.S., Heim, G., Hübner, W., Ilgen, P., et al. (2020). MICOS assembly controls mitochondrial inner membrane remodeling and crista junction redistribution to mediate cristae formation. EMBO J. 39, e104105. https://doi.org/10.15252/EMBJ.2019104105.

32. Oltersdorf, T., Elmore, S.W., Shoemaker, A.R., Armstrong, R.C., Augeri, D.J., Belli, B.A., Bruncko, M., Deckwerth, T.L., Dinges, J., Hajduk, P.J., et al. (2005). An inhibitor of Bcl-2 family proteins induces regression of solid tumours. Nature 7042, 677–681. https://doi.org/10.1038/nature03579.

33. Kotschy, A., Szlavik, Z., Murray, J., Davidson, J., Maragno, A.L., Le Toumelin-Braizat, G., Chanrion, M., Kelly, G.L., Gong, J.N., Moujalled, D.M., et al. (2016). The MCL1 inhibitor S63845 is tolerable and effective in diverse cancer models. Nature 7626, 477–482. https://doi.org/10.1038/nature19830.

34. van Delft, M.F., Wei, A.H., Mason, K.D., Vandenberg, C.J., Chen, L., Czabotar, P.E., Willis, S.N., Scott, C.L., Day, C.L., Cory, S., et al. (2006). The BH3 mimetic ABT-737 targets selective Bcl-2 proteins and efficiently induces apoptosis via Bak/Bax if Mcl-1 is neutralized. Cancer Cell 10, 389–399. https://doi.org/10.1016/J.CCR.2006.08.027.

35. Scaffidi, C., Fulda, S., Srinivasan, A., Friesen, C., Li, F., Tomaselli, K.J., Debatin, K.M., Krammer, P.H., and Peter, M.E. (1998). Two CD95 (APO-1/Fas) signaling pathways. EMBO J. 17, 1675–1687. https://doi.org/10.1093/EMBOJ/17.6.1675.

36. Pizzuto, M., and Pelegrin, P. (2020). Cardiolipin in immune signaling and cell death. Trends Cell Biol. 30, 892–903. https://doi.org/10.1016/J.TCB.2020.09.004.

37. Scorrano, L., Ashiya, M., Buttle, K., Weiler, S., Oakes, S.A., Mannella, C.A., and Korsmeyer, S.J. (2002). A distinct pathway remodels mitochondrial cristae and mobilizes cytochrome c during apoptosis. Dev. Cell 2, 55–67. https://doi.org/10.1016/S1534-5807(01)00116-2.

38. Frezza, C., Cipolat, S., Martins de Brito, O., Micaroni, M., Beznoussenko, G.V., Rudka, T., Bartoli, D., Polishuck, R.S., Danial, N.N., De Strooper, B., et al. (2006). OPA1 controls apoptotic cristae remodeling independently from mitochondrial fusion. Cell 126, 177–189. https://doi.org/10.1016/J.CELL.2006.06.025.

39. Sun, M.G., Williams, J., Munoz-Pinedo, C., Perkins, G.A., Brown, J.M., Ellisman, M.H., Green, D.R., and Frey, T.G. (2007). Correlated three-dimensional light and electron microscopy reveals transformation of mitochondria during apoptosis. Nat. Cell Biol. 9, 1057–1065. https://doi.org/10.1038/NCB1630.

40. Dalmonte, M.E., Forte, E., Genova, M.L., Giuffrè, A., Sarti, P., and Lenaz, G. (2009). Control of respiration by cytochrome c oxidase in intact cells: role of the membrane potential. J. Biol. Chem. 284, 32331–32335. https://doi.org/10.1074/JBC.M109.050146.

41. Kessler, R.J., Tyson, C.A., and Green, D.E. (1976). Mechanism of uncoupling in mitochondria: uncouplers as ionophores for cycling cations and protons. Proc. Natl. Acad. Sci. USA 73, 3141–3145. https://doi.org/10.1073/pnas.73.9.3141.

42. Scialò, F., Sriram, A., Fernández-Ayala, D., Gubina, N., Lõhmus, M., Nelson, G., Logan, A., Cooper, H.M., Navas, P., Enríquez, J.A., et al. (2016). Mitochondrial ROS Produced via reverse electron transport extend animal lifespan. Cell Metab. 23, 725–734. https://doi.org/10.1016/j.cmet.2016.03.009.

43. Riddell, F.G. (2002). Structure, conformation, and mechanism in the membrane transport of alkali metal ions by ionophoric antibiotics. Chirality 14, 121–125. https://doi.org/10.1002/CHIR.10052.

44. Jiang, X., and Wang, X. (2000). Cytochrome c promotes caspase-9 activation by inducing nucleotide binding to Apaf-1. J. Biol. Chem. 275, 31199–31203. https://doi.org/10.1074/JBC.C000405200.

45. Eguchi, Y., Srinivasan, A., Tomaselli, K.J., Shimizu, S., and Tsujimoto, Y. (1999). ATP-dependent steps in apoptotic signal transduction. Cancer Res. 59, 2174–2181.

46. Tasca, A., Helmstädter, M., Brislinger, M.M., Haas, M., Mitchell, B., and Walentek, P. (2021). Notch signaling induces either apoptosis or cell fate change in multiciliated cells during mucociliary tissue remodeling. Dev. Cell 56, 525–539.e6. https://doi.org/10.1016/J.DEVCEL.2020.12.005.

47. Blum, T.B., Hahn, A., Meier, T., Davies, K.M., and Kühlbrandt, W. (2019). Dimers of mitochondrial ATP synthase induce membrane curvature and self-assemble into rows. Proc. Natl. Acad. Sci. USA 116, 4250–4255. https://doi.org/10.1073/PNAS.1816556116.

48. Kondadi, A.K., Anand, R., and De Reichert, A.S. (2020). Cristae Membrane Dynamics – A Paradigm Change. Trends Cell Biol. 30, 923–936. https://doi.org/10.1016/J.TCB.2020.08.008.

49. Wolf, D.M., Segawa, M., Kondadi, A.K., Anand, R., Bailey, S.T., Reichert, A.S., van der Bliek, A.M., Shackelford, D.B., Liesa, M., and Shirihai, O.S. (2019). Individual cristae within the same mitochondrion display different membrane potentials and are functionally independent. EMBO J. 38, e101056. https://doi.org/10.15252/EMBJ.2018101056.

50. Galber, C., Minervini, G., Cannino, G., Boldrin, F., Petronilli, V., Tosatto, S., Lippe, G., and Giorgio, V. (2021). The f subunit of human ATP synthase is essential for normal mitochondrial morphology and permeability transition. Cell Rep. 35, 109111. https://doi.org/10.1016/j.celrep.2021.109111.

51. Pilic, J., Gottschalk, B., Bourgeois, B., Habisch, H., Koshenov, Z., Oflaz, F.E., Erdogan, Y.C., Miri, S.M., Yiğit, E.N., Aydın, M.Ş., et al. (2024). Hexokinase 1 forms rings that regulate mitochondrial fission during energy stress. Mol. Cell 84, 2732–2746.e5. https://doi.org/10.1016/J.MOLCEL.2024.06.009.

52. Erb, M., Hoffmann-Enger, B., Deppe, H., Soeberdt, M., Haefeli, R.H., Rummey, C., Feurer, A., and Gueven, N. (2012). Features of idebenone and related short-chain quinones that rescue ATP levels under conditions of impaired mitochondrial Complex I. PLoS One 7, e36153. https://doi.org/10.1371/JOURNAL.PONE.0036153.

53. Peruzzo, R., Corrà, S., Costa, R., Brischigliaro, M., Varanita, T., Biasutto, L., Rampazzo, C., Ghezzi, D., Leanza, L., Zoratti, M., et al. (2021). Exploiting pyocyanin to treat mitochondrial disease due to respiratory complex III dysfunction. Nat. Commun. 12, 2103. https://doi.org/10.1038/s41467-021-22062-x.

54. Pelegrin, P., Barroso-Gutierrez, C., and Surprenant, A. (2008). P2X7 receptor differentially couples to distinct release pathways for IL-1beta in mouse macrophage. J. Immunol. 180, 7147–7157. https://doi.org/10.4049/JIMMUNOL.180.11.7147.

55. Bussi, C., Heunis, T., Pellegrino, E., Bernard, E.M., Bah, N., Dos Santos, M.S., Santucci, P., Aylan, B., Rodgers, A., Fearns, A., et al. (2022). Lysosomal damage drives mitochondrial proteome remodelling and reprograms macrophage immunometabolism. Nat. Commun. 13, 7338. https://doi.org/10.1038/S41467-022-34632-8.

56. Foo, J., Bellot, G., Pervaiz, S., and Alonso, S. (2022). Mitochondria-mediated oxidative stress during viral infection. Trends Microbiol. 30, 679–692. https://doi.org/10.1016/J.TIM.2021.12.011.

57. Sefik, E., Qu, R., Junqueira, C., Kaffe, E., Mirza, H., Zhao, J., Brewer, J.R., Han, A., Steach, H.R., Israelow, B., et al. (2022). Inflammasome activation in infected macrophages drives COVID-19 pathology. Nature 7914, 585–593. https://doi.org/10.1038/s41586-022-04802-1.

58. Junqueira, C., Crespo, Â., Ranjbar, S., de Lacerda, L.B., Lewandrowski, M., Ingber, J., Parry, B., Ravid, S., Clark, S., Schrimpf, M.R., et al. (2022). FcγR-mediated SARS-CoV-2 infection of monocytes activates inflammation. Nature 7914, 576–584. https://doi.org/10.1038/s41586-022-04702-4.

59. Rodrigues, T.S., de Sá, K.S.G., Ishimoto, A.Y., Becerra, A., Oliveira, S., Almeida, L., Gonçalves, A.V., Perucello, D.B., Andrade, W.A., Castro, R., et al. (2021). Inflammasomes are activated in response to SARS-CoV-2 infection and are associated with COVID-19 severity in patients. J. Exp. Med. 218, e20201707. https://doi.org/10.1084/JEM.20201707.

60. Shang, C., Liu, Z., Zhu, Y., Lu, J., Ge, C., Zhang, C., Li, N., Jin, N., Li, Y., Tian, M., et al. (2022). SARS-CoV-2 causes mitochondrial dysfunction and mitophagy impairment. Front. Microbiol. 12, 4159. https://doi.org/10.3389/fmicb.2021.780768.

61. Gaidt, M.M., Ebert, T.S., Chauhan, D., Ramshorn, K., Pinci, F., Zuber, S., O'Duill, F., Schmid-Burgk, J.L., Hoss, F., Buhmann, R., et al. (2017). The DNA inflammasome in human myeloid cells is initiated by a STING-cell death program upstream of NLRP3. Cell 171, 1110–1124.e18. https://doi.org/10.1016/J.CELL.2017.09.039.

62. Mateo-Tórtola, M., Hochheiser, I.V., Grga, J., Mueller, J.S., Geyer, M., Weber, A.N.R., and Tapia-Abellán, A. (2023). Non-decameric NLRP3 forms an MTOC-independent inflammasome. Preprint at bioRxiv. https://doi.org/10.1101/2023.07.07.548075.

63. Ran, L., Ye, T., Erbs, E., Ehl, S., Spassky, N., Sumara, I., Zhang, Z., and Ricci, R. (2023). KCNN4 links PIEZO-dependent mechanotransduction to NLRP3 inflammasome activation. Sci. Immunol. 8, eadf4699. https://doi.org/10.1126/sciimmunol.adf4699.

64. Vince, J.E., De Nardo, D., Gao, W., Vince, A.J., Hall, C., McArthur, K., Simpson, D., Vijayaraj, S., Lindqvist, L.M., Bouillet, P., et al. (2018). The mitochondrial apoptotic effectors BAX/BAK activate caspase-3 and -7 to trigger NLRP3 inflammasome and caspase-8 driven IL-1β activation. Cell Rep. 25, 2339–2353.e4. https://doi.org/10.1016/j.celrep.2018.10.103.

65. Sarti, A.C., Vultaggio-Poma, V., Falzoni, S., Missiroli, S., Giuliani, A.L., Boldrini, P., Bonora, M., Faita, F., Di Lascio, N., Kusmic, C., et al. (2021). Mitochondrial P2X7 receptor localization modulates energy metabolism enhancing physical performance. Function (Oxf) 2, zqab005. https://doi.org/10.1093/FUNCTION/ZQAB005.

66. Martínez-García, J.J., Martínez-Banaclocha, H., Angosto-Bazarra, D., de Torre-Minguela, C., Baroja-Mazo, A., Alarcón-Vila, C., Martínez-Alarcón, L., Amores-Iniesta, J., Martín-Sánchez, F., Ercole, G.A., et al. (2019). P2X7 receptor induces mitochondrial failure in monocytes and compromises NLRP3 inflammasome activation during sepsis. Nat. Commun. 10, 2711. https://doi.org/10.1038/s41467-019-10626-x.

67. Fontana, M.F., and Vance, R.E. (2011). Two signal models in innate immunity. Immunol. Rev. 243, 26–39. https://doi.org/10.1111/J.1600-065X.2011.01037.X.

68. Hornung, V., Bauernfeind, F., Halle, A., Samstad, E.O., Kono, H., Rock, K.L., Fitzgerald, K.A., and Latz, E. (2008). Silica crystals and aluminum salts activate the NALP3 inflammasome through phagosomal destabilization. Nat. Immunol. 9, 847–856. https://doi.org/10.1038/NI.1631.

69. Suzuki, T., Okamoto, T., Katoh, H., Sugiyama, Y., Kusakabe, S., Tokunaga, M., Hirano, J., Miyata, Y., Fukuhara, T., Ikawa, M., et al. (2018). Infection with flaviviruses requires BCLXL for cell survival. PLoS Pathog. 14, e1007299. https://doi.org/10.1371/JOURNAL.PPAT.1007299.

70. Speir, M., Lawlor, K.E., Glaser, S.P., Abraham, G., Chow, S., Vogrin, A., Schulze, K.E., Schuelein, R., O'Reilly, L.A., Mason, K., et al. (2016). Eliminating Legionella by inhibiting BCL-XL to induce macrophage apoptosis. Nat. Microbiol. 1, 15034. https://doi.org/10.1038/nmicrobiol.2015.34.

71. Fritsch, M., Günther, S.D., Schwarzer, R., Albert, M.C., Schorn, F., Werthenbach, J.P., Schiffmann, L.M., Stair, N., Stocks, H., Seeger, J.M., et al. (2019). Caspase-8 is the molecular switch for apoptosis, necroptosis and pyroptosis. Nature 7784, 683–687. https://doi.org/10.1038/s41586-019-1770-6.

72. Newton, K., Wickliffe, K.E., Maltzman, A., Dugger, D.L., Reja, R., Zhang, Y., Roose-Girma, M., Modrusan, Z., Sagolla, M.S., Webster, J.D., et al. (2019). Activity of caspase-8 determines plasticity between cell death pathways. Nature *7784*, 679–682. https://doi.org/10.1038/s41586-019-1752-8.

73. Lawlor, K.E., Khan, N., Mildenhall, A., Gerlic, M., Croker, B.A., D'Cruz, A.A., Hall, C., Kaur Spall, S., Anderton, H., Masters, S.L., et al. (2015). RIPK3 promotes cell death and NLRP3 inflammasome activation in the absence of MLKL. Nat. Commun. *6*, 6282. https://doi.org/10.1038/ncomms7282.

74. Hughes, S.A., Lin, M., Weir, A., Huang, B., Xiong, L., Chua, N.K., Pang, J., Santavanond, J.P., Tixeira, R., Doerflinger, M., et al. (2023). Caspase-8-driven apoptotic and pyroptotic crosstalk causes cell death and IL-1β release in X-linked inhibitor of apoptosis (XIAP) deficiency. EMBO J. *42*, e110468. https://doi.org/10.15252/EMBJ.2021110468.

75. Nozaki, K., Maltez, V.I., Rayamajhi, M., Tubbs, A.L., Mitchell, J.E., Lacey, C.A., Harvest, C.K., Li, L., Nash, W.T., Larson, H.N., et al. (2022). Caspase-7 activates ASM to repair gasdermin and perforin pores. Nature *7916*, 960–967. https://doi.org/10.1038/s41586-022-04825-8.

76. Schneider, K.S., Groß, C.J., Dreier, R.F., Saller, B.S., Mishra, R., Gorka, O., Heilig, R., Meunier, E., Dick, M.S., Ćiković, T., et al. (2017). The inflammasome drives GSDMD-independent secondary pyroptosis and IL-1 release in the absence of caspase-1 protease activity. Cell Rep. *21*, 3846–3859. https://doi.org/10.1016/j.celrep.2017.12.018.

77. Ohto, U., Kamitsukasa, Y., Ishida, H., Zhang, Z., Murakami, K., Hirama, C., Maekawa, S., and Shimizu, T. (2022). Structural basis for the oligomerization-mediated regulation of NLRP3 inflammasome activation. Proc. Natl. Acad. Sci. USA *119*, e2121353119. https://doi.org/10.1073/PNAS.2121353119.

78. Chu, C.T., Ji, J., Dagda, R.K., Jiang, J.F., Tyurina, Y.Y., Kapralov, A.A., Tyurin, V.A., Yanamala, N., Shrivastava, I.H., Mohammadyani, D., et al. (2013). Cardiolipin externalization to the outer mitochondrial membrane acts as an elimination signal for mitophagy in neuronal cells. Nat. Cell Biol. *15*, 1197–1205. https://doi.org/10.1038/ncb2837.

79. Martinon, F., Pétrilli, V., Mayor, A., Tardivel, A., and Tschopp, J. (2006). Gout-associated uric acid crystals activate the NALP3 inflammasome. Nature *440*, 237–241. https://doi.org/10.1038/nature04516.

80. Drexler, S.K., Bonsignore, L., Masin, M., Tardivel, A., Jackstadt, R., Hermeking, H., Schneider, P., Gross, O., Tschopp, J., and Yazdi, A.S. (2012). Tissue-specific opposing functions of the inflammasome adaptor ASC in the regulation of epithelial skin carcinogenesis. Proc. Natl. Acad. Sci. USA *109*, 18384–18389. https://doi.org/10.1073/PNAS.1209171109.

81. Solle, M., Labasi, J., Perregaux, D.G., Stam, E., Petrushova, N., Koller, B.H., Griffiths, R.J., and Gabel, C.A. (2001). Altered cytokine production in mice lacking P2X(7) receptors. J. Biol. Chem. *276*, 125–132. https://doi.org/10.1074/JBC.M006781200.

82. Gross, O. (2012). Measuring the inflammasome. Methods Mol. Biol. *844*, 199–222. https://doi.org/10.1007/978-1-61779-527-5_15.

83. Petry, P., Aktories, P., Oschwald, A., and Kierdorf, K. (2024). Protocol for long-term monocultures of murine macrophages derived from distinct adult tissues. Star Protoc. *5*, 103145. https://doi.org/10.1016/J.XPRO.2024.103145.

84. Aktories, P., Petry, P., Glatz, P., Andrieux, G., Oschwald, A., Botterer, H., Gorka, O., Erny, D., Boerries, M., Henneke, P., et al. (2022). An improved organotypic cell culture system to study tissue-resident macrophages ex vivo. Cell Rep. Methods *2*, 100260. https://doi.org/10.1016/j.crmeth.2022.100260.

85. Walter, C., Marada, A., Suhm, T., Ernsberger, R., Muders, V., Kücükköse, C., Sánchez-Martín, P., Hu, Z., Aich, A., Loroch, S., et al. (2021). Global kinome profiling reveals DYRK1A as critical activator of the human mitochondrial import machinery. Nat. Commun. *12*, 4284. https://doi.org/10.1038/S41467-021-24426-9.

86. Sreekumar, A., Poisson, L.M., Rajendiran, T.M., Khan, A.P., Cao, Q., Yu, J., Laxman, B., Mehra, R., Lonigro, R.J., Li, Y., et al. (2009). Metabolomic profiles delineate potential role for sarcosine in prostate cancer progression. Nature *457*, 910–914. https://doi.org/10.1038/NATURE07762.

87. Lopez-Ibañez, J., Pazos, F., and Chagoyen, M. (2023). MBROLE3: improved functional enrichment of chemical compounds for metabolomics data analysis. Nucleic Acids Res. *51*, W305–W309. https://doi.org/10.1093/NAR/GKAD405.

STAR★METHODS

KEY RESOURCES TABLE

REAGENT or RESOURCE	SOURCE	IDENTIFIER
Antibodies		
anti-ASC (AL177), rabbit pAb	Adipogen	Cat# AG-25B-0006
anti-Caspase-1 (p20) (Casper-1), mouse mAb	Adipogen	Cat# AG-20B-0042
anti-NLRP3 (Cryo-2), mouse mAb	Adipogen	Cat# AG-20B-0014
anti-ATP5A1-F$_1$, mouse mAb	Abcam	Cat# ab14748
anti-GSDMD, rabbit mAb	Abcam	Cat# ab209845
anti-P2X7, rabbit mAb	Abcam	Cat# ab259942
anti-SOD2/MnSOD, rabbit mAb	Abcam	Cat# ab68155
anti-Akt, rabbit pAb	Cell Signaling	Cat# 9272
anti-Bak, rabbit mAb	Cell Signaling	Cat# 12105
anti-Caspase-3, rabbit pAb	Cell Signaling	Cat# 9662
anti-cleaved Caspase-3 (Asp175), rabbit pAb	Cell Signaling	Cat# 9661
anti-Caspase-9, mouse mAb	Cell Signaling	Cat# 9508
anti-Hsp60, rabbit mAb	Cell Signaling	Cat# 12165
anti-Vimentin, rabbit mAb	Cell Signaling	Cat# 5741
anti-Cytochrome c, rabbit pAb	Cell Signaling	Cat# 4272
anti-Cytochrome c, rabbit pAb	Abcam	Cat# ab90529
anti-VDAC1, rabbit mAb	Abcam	Cat# ab154856
anti-VDAC1, mouse mAb	Santa Cruz Biotechnology	Cat# sc-390996
anti-β-Actin, mouse mAb	Santa Cruz Biotechnology	Cat# sc-47778
anti-Bax, mouse pAb	Santa Cruz Biotechnology	Cat# sc-7480
anti-IL-1β/IL-1F2, goat pAb	R&D Systems	Cat# AF-401
anti-GAPDH, mouse mAb	R&D Systems	Cat# MAB5718
anti-FLAG, rabbit pAb	Sigma	Cat# F7425
anti-acetylated-α-tubulin, mouse mAb	Sigma	Cat# T6793
anti-Influenza A virus Nucleoprotein, rabbit pAb	GeneTex	Cat# GTX125989
anti-TGN38, rabbit mAb	Novus Biological	Cat# NBP1-03495
anti-ATP5F1-F$_O$, rabbit pAb	Proteintech	Cat# 15999-1-AP
anti-SARS-CoV Nucleocapsid (N) Protein, rabbit pAb	Rockland	Cat# 200-401-A50
anti-Digoxigenin AP, sheep pAb	Roche	Cat# 11093274910
horse anti-mouse IgG	Cell Signaling	Cat# 7076
goat anti-rabbit IgG	Cell Signaling	Cat# 7074
donkey anti-goat IgG	Invitrogen	Cat# A15999
goat anti-rabbit IgG	Jackson ImmunoResearch	Cat# 111035144
goat anti-mouse IgG	Jackson ImmunoResearch	Cat# 115035146
donkey anti-rabbit, Alexa Fluor 488	Jackson ImmunoResearch	Cat# 711-545-152
donkey anti-rabbit, Alexa Fluor 568	Invitrogen	Cat# A10042
goat anti-rabbit IgG (H+L), Alexa Fluor 647	Invitrogen	Cat# A21245
goat anti-mouse IgG (H+L), Alexa Fluor 488	Invitrogen	Cat# A11001
anti-Cytochrome c Alexa Fluor 647, mouse mAb	Biolegend	Cat# 612310
Bacterial and virus strains		
SARS-CoV-2 (B.1.1.7)	D. Hoffmann, M. Beer (Friedrich-Loeffler-Institut, Greifswald)	N/A
Modified Vaccinia Virus Ankara (MVA)	G. Sutter (LMU, Munich)	N/A

(Continued on next page)

Continued

REAGENT or RESOURCE	SOURCE	IDENTIFIER
A/Puerto Rico/8/1934 (H1N1)	This study	N/A
A/Puerto Rico/8/1934 delta NS1 (ΔNS1)	This study	N/A
Chemicals, peptides, and recombinant proteins		
Raptinal	Adipogen	Cat# AG-CR1-2902
Nigericin	Sigma-Aldrich	Cat# N7143
ATP	Sigma-Aldrich	Cat# A2383
poly(dA:dT)	Invivogen	Cat# tlrl-patn
Lipofectamin 2000	Invitrogen	Cat# 11668027
MSU crystals	Invivogen	Cat# tlrl-msu
Alum (Imject)	Thermo Fisher Scientific	Cat# 77161
E. coli K12 ultra-pure LPS	InvivoGen	Cat# tlrl-peklps
Fc-hFasL	gift from P. Schneider, Lausanne	N/A
Staurosporine	MedChem Express	Cat# HY-15141
tBid	R&D Systems	Cat# 882-B8-050
ABT-737	Selleckchem	Cat# S1002
S63845	Selleckchem	Cat# S8383
Gramicidin	Sigma-Aldrich	Cat# 50845
Ionomycin	Sigma-Aldrich	Cat# I0634
Nanchangmycin	Sigma-Aldrich	Cat# SML2251
Narasin	Sigma-Aldrich	Cat# NS1271
Maduramycin	Sigma-Aldrich	Cat# 34069
Salinomycin	Bio-techne	Cat# 3637
Imiquimod (R837)	InvivoGen	Cat# tlrl-imq
CL097	InvivoGen	Cat# tlrl-c97
Resiquimod (R848)	InvivoGen	Cat# tlrl-r848
Gardiquimod	InvivoGen	Cat# tlrl-gdq
Yoda-1	Sigma-Aldrich	Cat# SML1558
Rotenone	Sigma-Aldrich	Cat# R8875
Piericidin A	Enzo	Cat# ALX-380-235-M002
Metformin	Cayman	Cat# CAY13118-5
Antimycin A	Sigma-Aldrich	Cat# A8674
Sodium Azide	Sigma-Aldrich	Cat# S2002
KCN	Sigma-Aldrich	Cat# 60178
FCCP	Sigma-Aldrich	Cat# C2920
Oligomycin	Sigma-Aldrich	Cat# O4876
2-DG	Sigma-Aldrich	Cat# D8375
Idebenone	Sigma-Aldrich	Cat# I5659
Pyocyanin	Cayman	Cat# 10009594
KCl	Sigma-Aldrich	Cat# P9333
MCC950	Adipogen	Cat# AG-CR1-3615
PMA	Sigma-Aldrich	Cat# P1585
SPY700-DNA	Spirochrome	Cat# SC601
Fluoromount-G + DAPI	Invitrogen	Cat# 00495952
Protease inhibitor cocktail (PIC), cOmplete EDTA-free	Roche	Cat# 11873580001
Digitonin	Carl Roth	Cat# 4005
Digoxigenin-11-UTP	Roche	Cat# 3359247910
NBT/BCIP	Roche	Cat# 11681451001
Terminal Deoxynucleotidyl Transferase	Invitrogen	Cat# 10533065
CAS Blocking	Invitrogen	Cat# 00-8120

Continued

REAGENT or RESOURCE	SOURCE	IDENTIFIER
Osmium tetroxide, 4% aqueous solution	EMS	Cat# 19170
Glutaraldehyde	Sigma-Aldrich	Cat# G7651
Uranyl acetate	Science Services	Cat# E22400
Critical commercial assays		
Mouse IL-1β ELISA Kit	Invitrogen	Cat# 88-7013A-88
Human IL-1β ELISA Kit	Invitrogen	Cat# 88-7261-77
CellTiter-Glo Luminescent Cell Viability Assay	Promega	Cat# G7571
CytoTox 96 Non-Radio Cytotoxicity Assay	Promega	Cat# G1780
Pacific Blue Annexin V Apoptosis Detection Kit with 7 AAD	BioLegend	Cat# 640926
Zombie Aqua Fixable Viability Kit	BioLegend	Cat# 423102
Embed-812 Kit	Science Services	Cat# E14121
Deposited data		
Uncropped and combined dataset replicate immunoblot data	Mendeley	https://doi.org/10.17632/jrdrx955cn.1
Metabolite annotation	This study	N/A
Experimental models: Cell lines		
HCT116	ATCC	N/A
HeLa	Gift from K. Weber, Göttingen	N/A
HEK293T	ATCC	N/A
A549	ATCC	N/A
SK-HEP-1	ATCC	N/A
INS-1 (832/12)	C.B. Newgard (Duke University SOM)	https://doi.org/10.2337/DIABETES.49.3.424
SV40-MEF	A. Rambold, Freiburg	N/A
Vero E6	ATCC	N/A
U2OS	ATCC	N/A
THP-1	ATCC	N/A
THP-1 NLRP3 KO	Invivogen	N/A
HCT116 $BAX^{-/-}$ $BAK^{-/-}$	R. Youle (NIH, Bethesda)	https://doi.org/10.1038/ONC.2011.497
HeLa $IMMT^{-/-}$	S. Jakobs, Göttingen; Stephan et al.[31]	https://doi.org/10.15252/EMBJ.2019104105
MEF AOX	A. Akhtar, Freiburg	https://doi.org/10.1038/S42255-023-00904-W
Murine bone marrow-derived macrophages (BMDMs)	This study	N/A
Murine bone marrow-derived dendritic cells (BMDCs)	This study	N/A
Murine microglia	This study	N/A
Murine Kupffer cells	This study	N/A
Murine thymocytes	This study	N/A
Human peripheral blood mononuclear cells (PBMCs)	This study	N/A
Human monocyte derived macrophages (MDMs)	This study	N/A
Experimental models: Organisms/strains		
Mice, C57BL/6 background, wild-type	CEMT, Freiburg	N/A
Mice, C57BL/6 background, $Nlrp3^{-/-}$	J. Tschopp, Lausanne; Martinon et al.[79]	https://doi.org/10.1038/nature04516

Continued

REAGENT or RESOURCE	SOURCE	IDENTIFIER
Mice, C57BL/6 background, *Pycard*^{-/-}	J. Tschopp, Lausanne; Drexler et al.[80]	https://doi.org/10.1073/PNAS.1209171109
Mice, C57BL/6 background, *P2rx7*^{-/-}	Gift of P. Stachon, Freiburg; Solle et al.[81]	RRID:IMSR_JAX:005576; https://doi.org/10.1074/JBC.M006781200
Xenopus laevis, wild-type	European Xenopus Resource Centre (EXRC), or Xenopus 1	N/A
Recombinant DNA		
AT1.03	H. Imamura and H. Noji, Osaka	Addgene #51958; [https://doi.org/10.1073/PNAS.0904764106]
mtAT1.03	H. Imamura and H. Noji, Osaka	[https://doi.org/10.1073/PNAS.0904764106]
Software and algorithms		
GraphPad PRISM, v9	GraphPad Software	N/A
FlowJo, v10	BD Biosciences	N/A
SparkControl magellan, v3.1	Tecan	N/A
Leica Application Suite X, v3.5.1	Leica Microsystems	N/A
ZEN software black edition, v2.6	Carl Zeiss Microscopy	N/A
Zeiss Zen Pro Blue	Carl Zeiss Microscopy	N/A
Imaris, vx64 9.6.0	Oxford Instruments	N/A
ImageJ Fiji	http://fiji.sc	N/A
Amira, v6.0.1	Thermo Fisher Scientific	N/A
3dmod	J.R. McIntosh, Boulder (http://bio3d.colorado.edu/imod/)	https://doi.org/10.1006/JSBI.1996.0013
DIVA, v7	BD Biosciences	N/A
Wave software, v2.6.1	Agilent	N/A
Sartorius IncuCyte Analysis, 2022	Sartorius	N/A
MATLAB, v9.11.0.1769968 [R2021b]	The Mathworks Inc	N/A
Adobe Photoshop	Adobe	N/A
Adobe Illustrator	Adobe	N/A

EXPERIMENTAL MODEL AND STUDY PARTICIPANT DETAILS

Mice

Nlrp3^{-/-},[79] *Pycard*^{-/-},[80] *P2rx7*^{-/-},[81] and wild-type mice of C57BL/6 background were housed under SPF conditions at the Center for Experimental Models and Transgenic Services (CEMT, Freiburg, Germany) in accordance with local guidelines.

BMDM and BMDC preparation

Murine bone marrow-derived dendritic cells (BMDCs) and macrophages (BMDMs) were differentiated from tibial and femoral bone marrow as previously described in detail.[82] Male and female mice were used between the age of 8-30 weeks. Cells were cultured at 37°C, 5% CO_2 in a humidified incubator in RPMI1640 containing GlutaMAX (Gibco) supplemented with 10% FCS, 100 U ml^{-1} penicillin-streptomycin, and recombinant murine GM-CSF (BMDCs) or human M-CSF (BMDMs, both Immunotools) at 20 ng ml^{-1} or 100 ng ml^{-1}, respectively. After 6-8 days of differentiation, cells were detached and plated at a density of 0.7-1 x 10^5 cells per 96-well the day before the experiment.

Cell lines

Cell lines were cultured in T75 flasks at 37°C, 5% CO_2 in a humidified incubator and continuously passaged. Human HeLa, HEK293, A549, SK-HEP1, mouse embryonic fibroblast (MEF), and simian Vero E6 cells were cultured in DMEM, high glucose, L-glutamine, sodium pyruvate. Human HCT116 and U2OS cells were grown in McCoy's 5a Medium. Murine INS-1 cells were cultured in RPMI-1640 supplemented with 2 mM L-glutamine, 10mM HEPES, 1 mM sodium pyruvate, and 50 μM 2-mercaptoethanol. Human THP-1 cells were cultured in RPMI1640 containing GlutaMAX (all Gibco). For differentiation, 100 ng ml^{-1} PMA (Sigma-Aldrich) was added. Media were supplemented with 10% fetal calf serum (FCS) and 100 U ml^{-1} penicillin-streptomycin (both Gibco). SV40 MEFs were cultured without penicillin-streptomycin. Unless indicated otherwise, cells were seeded at a density of 2.2 x 10^5 (THP-1) or 6-9 x 10^4 cells cm^{-2} the day before the experiment.

Preparation of PBMCs and MDMs

Human peripheral blood mononuclear cells (PBMCs) were isolated from venous blood of seven healthy female or male donors with a median age of 34 years (Ethik-Kommission Universitätsklinikum Freiburg, reference number 20-1109) by density gradient centrifugation with a Ficoll Paque Plus (Cytiva) gradient. Isolated cells were cultured at 37°C and 5% CO_2. For PBMC experiments, cells were rested for 2 h after isolation in RPMI containing GlutaMAX (Gibco) without supplements. Non-adherent cells were washed away and cells were rested in BMDM medium overnight before being used for experiments. To obtain monocyte-derived macrophages (MDMs), human PBMCs were rested overnight in BMDM medium. Then, non-adherent cells were washed away and fresh BMDM medium was added. Cells were cultured for 7 to 8 days. Medium was changed every second day.

Preparation of primary thymocytes

Primary murine thymocytes were isolated by removing the thymus from euthanized mice and mashing it through a 100 μm nylon cell strainer (Corning). Single-cell suspensions were collected in RPMI1640 containing GlutaMAX supplemented with 10% FCS, 100 U ml^{-1} penicillin-streptomycin and erythrocytes were lysed using red blood cell lysis buffer (BioLegend). For stimulation, 0.2×10^6 cells per 96-well were seeded.

Preparation of microglia

Murine microglia were obtained and cultured as previously described.[83,84] In brief, the whole brain was removed and homogenized in a glass potter filled with 10 ml cold dissection medium (HBSS, 1.5% HEPES, 1.3% Glucose). The single cell suspension was transferred through a 70 μm cell strainer. Cells were centrifuged (10 min, 400 g_n, 4°C). The supernatant was discarded and a density gradient (37% Percoll) was performed. The resulting cell pellet was washed with PBS and centrifuged (5 min, 300 g_n, 4°C). The cell pellet was resuspended in 10 ml microglia medium (DMEM, 10% FCS, 1% P/S [all Gibco], CSF-1 20 ng ml^{-1} [PeproTech], IL-34 ng ml^{-1} [BioLegend]) and plated into polyethyleniminie (PEI)-coated T25 flasks. Three brains were cultured per flask. Medium was changed after 2 days of culture. Assays were performed after 2 weeks of culture. Cells were cultured at organotypic oxygen conditions (3% O_2, 5% CO_2, 92% N_2).

Preparation of Kupffer cell

Murine Kupffer cells were obtained and cultured as previously described.[83,84] In brief, the liver was removed and washed with PBS. An enzymatic digestion (PBS, 4% FCS [both Gibco], 0.2 mg ml^{-1} DNase, 1 mg ml^{-1} Collagenase [both Sigma-Aldrich]) was performed and the liver was homogenized. The cell suspension was passed through a 100 μm strainer. Cells were then centrifuged (10 min, 400 g_n, 4°C) and a density gradient centrifugation (37% Percoll) was performed. The resulting cell pellet was washed with PBS and centrifuged (5 min, 300 g_n, 4°C). The supernatant was discarded and red blood cell lysis was performed. Cells were centrifuged (5 min, 300 g_n, 4°C), the cell pellet was resuspended in 10 ml Kupffer cell medium (DMEM, 10% FCS, 1% P/S [all Gibco], CSF-1 20 ng ml^{-1} [Peprotech]) and plated in PEI-coated T25 flasks. One liver was cultured per flask. Medium was changed after 2 days of culture. Assays were performed after 2 weeks of culture. Cells were cultured at organotypic oxygen conditions (3% O_2, 5% CO_2, 92% N_2).

Xenopus animal culture

Wild-type *Xenopus laevis* were obtained from the European Xenopus Resource Centre (EXRC) at University of Portsmouth, School of Biological Sciences, UK, or Xenopus 1, USA. Frog maintenance and care was conducted according to standard procedures in the AquaCore facility, University Freiburg, Medical Center (RI_00544). This work was done in compliance with German animal protection laws and was approved under Registrier-Nr. G-18/76 by the state of Baden-Württemberg. Drug treatment of embryos started at stage 39/40.

METHOD DETAILS

Inflammasome stimulation

NLRP3 inflammasome stimulations were performed as described in detail.[82] In brief, myeloid cells were primed with 20-50 ng ml^{-1} *E. coli* K12 ultra-pure lipopolysaccharide (LPS, InvivoGen) for 3 h, and treated with inflammasome activators for 15 min-6 h. Stimulations were performed in technical triplicates. Inflammasome activators and stimuli were typically used as follows: 2.5 mM ATP, 5-10 μM nigericin (nig.), narasin, or nanchangmycin, 2-5 μM gramicidin, 20 μM ionomycin, 10-20 μM maduramycin (all Sigma-Aldrich), or salinomycin (Bio-techne), 200 μM imiquimod (R837), CL097, gardiquimod, 200-400 μM resiquimod (R848) (all InvivoGen), and 10 or 30 μM Yoda-1 (Sigma-Aldrich). Crystals were added at 0.25 (monosodium urate crystals, MSU) or 0.3 μg ml^{-1} (aluminum hydroxide particles, alum). For activation of the AIM2 inflammasome, 2 μg ml^{-1} poly(dA:dT) (Invivogen) were transfected using Lipofectamine 2000 (Invitrogen) in Opti-MEM medium (Gibco) according to the manufacturer's instructions. Inhibitors of glycolysis and the ETC as well as of ATP synthase, and mitochondrial uncouplers were typically used as follows: 5 or 20 mM 2-deoxy-D-glucose (2-DG), 2-10 μM piericidin (Enzo), rotenone, or antimycin A (AA), 1-3 μM oligomycin, 5 μM carbonyl cyanide-p-trifluoromethoxyphenylhydrazone (FCCP), 1 mM potassium cyanide (KCN) or sodium azide (NaN$_3$) (all Sigma-Aldrich), and 50 mM metformin (Cayman). Inhibitors were added 30 min before (MCC950, 3 μM, Adipogen) or at the same time as the stimuli (KCl, 50 mM, Sigma-Aldrich).

Apoptosis induction and co-stimulation

For apoptosis induction, cells were treated with different activators for the indicated times. Time point of analysis and dose of apoptosis inducer were optimized for each cell type or cell line individually and typically used as follows: 5-10 μM raptinal (Rap., Adipogen), 100 ng ml⁻¹ FC-hFasL (gift from Pascal Schneider, Lausanne), 20 μM staurosporine (MedChem Express), 1 μM ABT-737, 5 μM S63845 (both Selleckchem). To assess apoptosis inhibition, respective stimuli were added together with the apoptosis inducer, if not indicated otherwise. Idebenone (25 μM, Sigma-Aldrich) and pyocyanin (50 μM, Cayman) were added 30 min before raptinal.

Viral infection

Vero E6 cells were seeded (2.4 x 10⁵ cells per 24-well) and infected with authentic SARS-CoV-2 (B.1.1.7, MOI: 1), diluted in OptiMEM (250 μl per well). One hour after infection (hpi) (37°C, 5% CO₂), inoculum was exchanged for 500 μl per well SARS-CoV-2 medium (DMEM, supplemented with 100 U ml⁻¹ penicillin-streptomycin, 250 mM HEPES [both Gibco], 1% NaHCO₃, 2% FCS). Cells were cultured at 37°C, 5% CO₂. At 17 hpi, cells were treated with raptinal.

HeLa cells were seeded (3 x 10⁵ cells per 6-well) 4 h prior to infection. Thereafter, cells were infected with Modified Vaccinia Ankara (MVA, MOI: 2), diluted in 1 ml per well fresh RPMI1640 containing 10% FCS. Cells were cultured at 37°C and 5% CO₂. 14.5 hpi, cells were treated with raptinal.

Differentiated human MDMs were infected with A/Puerto Rico/8/1934/(H1N1) (H1N1), or a H1N1 mutant with a deletion in the NS1 protein (H1N1-ΔNS1) (MOI: 1 or 10) in infection medium (RPMI1640 containing 0.2% BSA, 100 U ml⁻¹ penicillin and 100 μg ml⁻¹ streptomycin (all Sigma-Aldrich)) with 1 μg ml⁻¹ TPCK-treated trypsin in the presence or absence of LPS (50 ng ml⁻¹). Medium was changed 2 hpi. 9-12 hpi cells were treated with 5 μM raptinal. Cell-free supernatants or cell lysates were collected at the indicated times.

Immunodetection of proteins

Released cytokines were quantified from cell-free supernatants using ELISA kits for murine or human IL-1β (Thermo Fisher Scientific [Invitrogen]) according to the manufacturer's instructions and as previously described.[82] ELISA data is depicted as mean ±SD of technical triplicates.

For immunoblot analysis, cell-free supernatant and cell lysate samples in SDS- and DTT-containing sample buffer were analyzed. Triplicates were pooled and proteins were separated by SDS-PAGE and transferred to nitrocellulose membranes using standard techniques.[82] The following primary antibodies were used: anti-Caspase-1 (p20) mAb (Casper-1), anti-NLRP3 mAb (Cryo-2), anti-ASC pAb (AL177) (all Adipogen), anti-ATP5A1-F₁ mAb, anti-GSDMD mAb, anti-P2X₇ mAb (EPR24130-77), anti-SOD2/MnSOD mAb (EPR2560Y) (all Abcam), anti-Akt pAb (#9272), anti-Bak mAb (#12105), anti-Caspase-3 pAb (#9662), anti-cleaved Caspase-3 (Asp175) pAb (#9661), anti-Caspase-9 mAb (#9508), anti-Vimentin mAb (#5741) (all Cell Signaling), anti-Cytochrome c pAb (#4272, Cell Signaling and ab90529, Abcam), anti-VDAC1 mAb (EPR10852(B), Abcam and sc-390996, Santa Cruz Biotechnology), anti-Bax pAb (sc-493), anti-β-Actin mAb (sc-47778) (both Santa Cruz Biotechnology), anti-IL-1β/IL-1F2 pAb, anti-GAPDH mAb (MAB5718) (all R&D Systems), anti-FLAG pAb (Sigma), anti-Influenza A virus Nucleoprotein pAb (GeneTex), anti-ATP5F1-F₀ pAb (Proteintech), anti-SARS-CoV Nucleocapsid (N) Protein (200-401-A50, Rockland).

Signal intensities were determined by calculating the mean luminescence intensities of individual bands using Photoshop (Adobe, Version 11 and 23). For every lane, an equal area was determined including all of the signal and a minimal amount of background. An equal empty area was measured to subtract the background from all signal measurements. If not indicated otherwise, measured values were corrected to their loading control. Supernatant samples were not corrected. Exposure times were used at which the signals of interest were not saturated. For better visualization, longer exposures of the same raw data are shown in the figures.

Cell viability assays

Lytic cell death was assessed by measuring activity of released LDH in cell-free supernatants using a colorimetric assay (Promega) according to the manufacturer's protocol. Medium without cells served as blank value which was subtracted from all other values. Results are shown as percentage of 100% dead cells lysed with lysis buffer 45 min prior to collection of the cell supernatants.

Intracellular ATP was quantified using the CellTiter-Glo Luminescent Cell Viability Assay (Promega) according to the manufacturer's protocol. Luminescence was recorded and depicted as relative light units (RLU), or relative to control cells.

Cell death characterization by flow cytometry

Cell death was assessed by flow cytometry using the Pacific Blue Annexin V Apoptosis Detection Kit with 7-AAD (BioLegend) or an antibody specific for cleaved caspase-3. In brief, for Annexin V/7-AAD staining, treated cells were harvested with HBSS containing 0.5 mM EDTA (BMDCs), 0.05% trypsin-EDTA (HCT116 cells), or gentle resuspension (thymocytes) and transferred to 96-well V-bottom plates. Cells were washed and stained with Pacific Blue Annexin V and 7-AAD in Annexin V binding buffer according to the manufacturer's protocol. For measurement of cleaved caspase-3, cells were harvested with 0.05% trypsin-EDTA, fixed with 4% paraformaldehyde (PFA) for 20 min, and permeabilized using a saponin containing permeabilization buffer (PBS, 0.5% saponin, 0.5% BSA). Cells were stained with a cleaved-caspase-3 antibody (Asp175, #9661, Cell Signaling) overnight at 4°C in permeabilization buffer and subsequently with an Alexa Fluor 488-labeled donkey anti-rabbit (711-545-152, Jackson ImmunoResearch) secondary antibody for 1 h at room temperature in permeabilization buffer. After staining, the cells were pelleted, resuspended in

Annexin V binding buffer (for Annexin V/7-AAD-stained cells) or PBS (for cleaved caspase-3-stained cells), and analyzed with a BD FACSCanto II (BD Biosciences) flow cytometer. Data were acquired with DIVA (BD Biosciences, Version 7) and analyzed with FlowJo software (FlowJo LLC, BD Version 10).

Incucyte live cell imaging
SK-Hep1 cells were seeded at a density 2×10^4 cells per 96-well and incubated for 24 h. Then, cells were washed with PBS and replenished with media containing live cell dye (SPY700-DNA, Spirochrome, #SC601) and incubated for 2 h. Together with the experimental treatment, 20 ng per well propidium iodide was added to stain dead cells. All treatments were done in technical triplicates. The plates were then moved into an IncuCyte SX5 system (Essen Bioscience) and images were recorded every hour using a 20 × objective in bright-field, near-infrared, and orange channels. The cell death kinetics were analyzed using Sartorius IncuCyte Analysis software.

MOMP in isolated mitochondria
For subcellular fractionation into a soluble cytoplasmatic and an insoluble fraction containing mitochondria, HCT116 cells or MEFs were harvested, washed with PBS, and cell pellets were resuspended in SEM buffer (10 mM HEPES pH 7.2, 250 mM sucrose) supplemented with protease inhibitor cocktail (PIC, cOmplete EDTA-free, Roche). Cells were disrupted in two runs of 15 passages through a 25G needle on a 1 ml syringe. Lysates were cleared from debris and intact cells by centrifugation (5 min, 800 g_n). The suspension was centrifuged (30 min, 13,000 g_n, 4°C). The resulting pellet, representing the insoluble fraction containing mitochondria, was washed twice in SEM buffer and once in KCl buffer (125 mM KCl, 4 mM MgCl$_2$, 5 mM Na$_2$HPO$_4$, 5 mM succinate, 5 μM rotenone, 0.5 mM EGTA, 15 mM HEPES–KOH, pH 7.4) supplemented with PIC. Isolated mitochondria were incubated with or without 50 μM nigericin and/or 10 nM tBID (R&D Systems) or solvent control for 10 min at 37°C. Subsequently, mitochondria were separated from the soluble fraction (5 min, 13,000 g_n, 4°C). SDS- and DTT-containing sample buffer was added and both fractions were subjected to immunoblot analysis.

Cytochrome c release assay
Cytochrome c release was determined by immunoblot analysis or flow cytometry. For immunoblot analysis, digitonin-permeabilized cells were fractionated into a soluble cytoplasmic fraction and an insoluble fraction containing mitochondria. HCT116 were seeded at a density of 9 x 10^5 cells per 6-well and cultured overnight. Cells were treated as indicated, detached with 0.05% trypsin-EDTA, pelleted (5 min, 500 g_n, 4°C), washed with cold PBS, again pelleted, and resuspended in 200 μl permeabilization buffer (100 μg ml^{-1} digitonin [Carl Roth], 75 mM NaCl, 8 mM Na$_2$HPO$_4$, 250 mM sucrose, PIC) per condition and lysed for 5 min on ice. After centrifugation (5 min, 21,000 g_n, 4°C), a 100 μl sample from the cell-free supernatant, representing the soluble fraction, was taken and mixed with 3x SDS and DTT-containing sample buffer. The mitochondria-containing pellet was washed twice with cold PBS containing PIC (5 min, 21,000 g_n, 4°C) and lysed in 150 μl 1x SDS- and DTT-containing sample buffer. Samples were subjected to immunoblot analysis.

For flow cytometry analysis, BMDMs were seeded at a density of 8 x 10^4 cell per 96-well and cultured overnight. Cells were pre-treated with 50 mM KCl, if indicated, followed by compound stimulation for 90 min. Thereafter, cells were detached using HBSS/ETDA, pelleted (5 min, 400 g_n, 4°C), washed with cold PBS, again pelleted, and stained (30 min, RT, in the dark) with Zombie Aqua dye (Zombie Aqua Fixable Viability Kit, BioLegend). Stained cells were washed with cold PBS, resuspended in 200 μl permeabilization buffer (50 μg ml^{-1} digitonin, PBS, 100 mM KCl) and lysed for 5 min on ice. Thereafter, cells were pelleted and resuspended in 4% PFA in PBS (20 min, RT, in the dark). Fixed cells were pelleted, resuspended in 200 μl blocking buffer (2% FCS in PBS, containing 0.05% saponin), washed and stained with Alexa Fluor 647 anti-Cytochrome c antibody (Biolegend; 20 min, RT) in blocking buffer. After one wash (2% FCS in PBS), cells were analyzed with a LSRFortessa (BD Biosciences) flow cytometer. Data were acquired with DIVA (BD Biosciences, Version 7) and analyzed with FlowJo software (FlowJo LLC, BD, Version 10).

Digitonin-mediated MOMP
To determine cytochrome c availability for release from mitochondria, the outer mitochondrial membrane was permeabilized using intact cells with a carefully titrated digitonin concentration. HCT116 cells were seeded at a density of 6.3 x 10^6 cells per T75 flask and cultured overnight. After the experimental treatment in T75 flasks, cells were detached with 0.05% trypsin-EDTA. Cells from several flasks of the same treatment condition (untreated or nigericin-treated) were pooled to minimize batch effects and pelleted (5 min, 500 g_n, 4°C). Cells were resuspended in cold PBS and split into separate samples (typically nine samples per initial T75 flask) for lysis under different conditions. Pelleted cells were resuspended in 200 μl permeabilization buffer (75 mM NaCl, 8 mM Na$_2$HPO$_4$, 250 mM sucrose, PIC) containing the indicated concentrations of digitonin (between 100 μg ml^{-1} and 4000 μg ml^{-1}) for 10 min on ice. After centrifugation (5 min, 21,000 g_n, 4°C), a 100 μl sample from the cell-free supernatant, representing the soluble fraction, was taken and mixed with 3x SDS and DTT-containing sample buffer. The mitochondria-containing pellet was washed twice with cold PBS containing PIC (5 min, 21,000 g_n, 4°C) and lysed in 150 μl 1x SDS- and DTT-containing sample buffer. Samples were subjected to immunoblot analysis.

Blue Native PAGE of isolated mitochondria
HEK293T cells were stimulated with nigericin, oligomycin, or vehicle for 12 h. Mitochondria were isolated as previously described.[85] In brief, cell pellets were homogenized in solution A (220 mM mannitol, 70 mM sucrose, 20 mM HEPES-KOH, pH 7.6, 1 mM EDTA,

0.5 mM PMSF and 2 mg ml^{-1} BSA) using a glass potter. Cellular debris was removed by centrifugation (5 min, 800 g_n, 4°C) and mitochondria were isolated from the recovered supernatant by centrifugation (10 min, 10,000 g_n, 4°C). Mitochondrial pellet was resuspended in solution B (solution A without BSA) and centrifuged (5 min, 800 g_n, 4°C). Mitochondria were pelleted (15 min, 10,000 g_n, 4°C) and resuspended in sucrose buffer (10 mM HEPES pH 7.6, 0.5 M sucrose). Protein concentrations were determined by Bradford assay. Thereafter, respiratory chain complexes were analyzed by Blue Native PAGE. Isolated mitochondria were solubilized (1% [w/v] digitonin, 20 mM Tris/HCl, pH 7.4, 0.1 mM EDTA, 10% [v/v] glycerol, 50 mM NaCl) and incubated (15 min) on ice. Samples were centrifuged (10 min, 20,800 g_n, 4 °C) and supernatant was loaded on 4-10% continuous gradient Blue Native gels followed by electrophoresis and immunoblotting.

Brightfield imaging
For live cell imaging, HCT116 cells were plated at a density of 7 x 10^4 cells per well in 8-well μ-slides (IbiTreat, Ibidi). Cells were treated with compounds as indicated and imaged at 37°C in a 5% CO$_2$ humidified atmosphere. Microscopy was performed with a Leica SP8 confocal microscope equipped with a 20×/0.75 oil objective (Leica Microsystems). Images were processed using Leica Application Suite X (Leica Microsystems, Version 3.5.1).

Immunofluorescence and confocal imaging
MEFs were seeded on fibronectin-coated coverslips and treated as indicated. Cells were fixed for 15 min in 4% PFA and subsequently permeabilized with 0.2% Triton X-100 in PBS for 15 min. Free protein binding sites were blocked with blocking buffer (5% FCS, 0.1% Tween 20, in PBS) for 1 h. Coverslips were incubated with primary antibodies (anti-Hsp60 XP, Cell Signaling, #12165) diluted in blocking buffer for 16 h at 4°C. Secondary antibody staining (donkey anti-rabbit Alexa Fluor 568, Invitrogen, #A10042) was performed in blocking buffer for 1 h. Samples were mounted in Fluoromount-G containing DAPI (Invitrogen, #00495952). Images were acquired using a Zeiss 780 laser confocal scanning microscope equipped with a 63×/1.4 NA objective and ZEN software black edition (Carl Zeiss Microscopy, v.2.6). Images were processed and brightness and contrast were adjusted using Fiji ImageJ.

THP-1 *NLRP3$^{-/-}$* stably expressing NLRP3-mNG were seeded on coverslips (12 mm) in a 24-well plate with PMA (100 ng ml^{-1}) overnight. Medium was renewed the next day. After a 24 h rest period, cells were treated as indicated for 1 h. MCC950 was added if cells were treated with CL097. After treatment, cells were fixed in 4 % PFA in PBS (37°C, 15 min), washed with PBS (3x, 5min) and permeabilized in 0.05 % saponin in PBS for 5 min. Cells were then blocked in blocking buffer (2 % BSA, 0.05 % saponin in PBS) for 1 h. Then, cells were stained with primary anti-TGN38 mAb (Novus Biological, NBP1-03495) for 2 h to overnight at RT and goat anti-Rabbit IgG (H+L), Alexa Fluor 647 (Invitrogen, A-21245) for 1 h at RT in blocking buffer. Staining of the nuclei was performed with Hoechst 33342 (Invitrogen, 21492). Cells were imaged using a Plan-Apochromat 63×/1.4 oil objective on a Zeiss LSM800 confocal system equipped with an Airyscan module and controlled by the Zen blue software.

The number of nuclei was determined by enumerating the nuclei using the "Analyze Particles" plugin after segmenting the Hoechst 33342 signal through automatic thresholding in Fiji. To estimate the number of TGN-located speckles, a mask was created for the TGN signal in each cell, and NLRP3 speckles were counted within these regions following automatic thresholding. Finally, a ratio between the TGN-located NLRP3 speckles and the nuclei was calculated.

Transmission electron microscopy
Aclar disks were punched with 18 mm diameter using 0.198 mm thick aclar films (Plano) and sterilized with 70% ethanol before usage. On these, cells were grown to ~70% confluency. Control and treated samples were immobilized and fixed with 2.5% glutaraldehyde in 0.1 M cacodylate buffer at pH 7.4, first for 1 h at room temperature, then transferred to 4°C until the next day. Before post-fixation, the cells were additionally stained with 1% osmium tetroxide and 1.5% K$_4$[Fe(CN)$_6$] in 0.1 M cacodylate buffer at pH 7.4 for 1 h at room temperature. Following post-fixation in 1% osmium tetroxide for 1 h at room temperature and pre-embedding en-bloc staining with 1% uranyl acetate for 30 min at room temperature, samples were dehydrated and embedded in Agar 100 resin (Plano).

For 2D analysis, ultrathin sections of ~ 70 nm thickness were recorded on a Philips CM120 BioTwin transmission electron microscope (Philips Inc.). Usually, 2D images of at least 20 different cells were randomly recorded for each sample at 8600× original magnification using a TemCam 224A slow scan CCD camera (TVIPS). Recordings of thin sections were processed in Fiji ImageJ using the median filter.

For electron tomography, thin sections of ~ 230 nm that were additionally decorated with 10 nm gold beads on both sides were recorded on a Talos L120C transmission electron microscope (Thermo Fischer Scientific/FEI company) at 17,500× original magnification using a Ceta 4k × 4k CMOS camera in unbinning mode. Series were recorded from -65.0° to 65.0° with a 3° dose-symmetric angular increase. The series were calculated using Etomo (David Mastronade, http://bio3d.colorado.edu/). Tomograms were processed using the nonlinear anisotropic diffusion (NAD) filter in IMOD (David Mastronade, http://bio3d.colorado.edu/imod/). Models were generated in IMOD from mitochondria where the inner mitochondrial membrane (IMM) was clearly visible over most of the recorded z-stack. To determine the cristae junction (CJ) density, the IMM and CJ areas were tagged, the included areas were determined, and a ratio of CJ to IMM area was calculated. Models were processed and visualized in Amira (Thermo Fisher Scientific, Version 6.0.1).

Classification of mitochondrial ultrastructure

Mitochondrial architecture was assessed based on transmission electron microscopy images. Mitochondria were characterized based on their cristae structure.[31] Mitochondria were classified as wildtype/lamellar with high or reduced degree of order if they showed classical lamellar cristae which presented in parallel sheets. All mitochondria that showed different cristae shapes or that were highly disordered were classified to be aberrant. Aberrant cristae included onion-shaped, arc-shaped, one-membrane, two-membrane, and stack-like architectures.

Measurement of cellular potassium levels

BMDMs were detached and 15×10^6 cells per condition were resuspended in BMDM medium. Compounds were added and cells were incubated for 1 h (37°C, 5% CO_2). After treatment, cells were pelleted (5min, 400 g_n, 4°C), resuspended in 1 ml 0.9% NaCl per condition and lysed by three freeze/thaw cycles. Lysed cells were centrifuged (10 min, 13,000 g_n, RT) and K^+ concentrations in the supernatants were analyzed using an ion-selective electrode (ISE unit) of a cobas8000 clinical analyzer (Roche Diagnostics). Intracellular K^+ levels are depicted relative to untreated controls.

Subcellular ATP measurements

For ATP measurement in HeLa or INS1, cells were seeded in 6-well plates on 30 mm glass coverslips (Paul Marienfeld). AT1.03 or mtAT1.03 was transfected using PolyJet (SignaGen Laboratories). Per well, 3 μl of PolyJet reagent was mixed with 1 μg of plasmid DNA in 100 μl of DMEM devoid of serum and antibiotics. The transfection mixture was added to 1 ml of culture medium for 8 h and was then replaced with 2 ml of culture medium. Imaging was performed 48 h after transfection.

Medium was changed, cells were treated as indicated and ATP FRET-imaging was performed with an inverted microscope (Nikon Eclipse Ti2) equipped with a 40×/1.15 NA water immersion objective (CFI Apochromat, Nikon), full-multiband filter set (BrightLine, Semrock), and two Kinetix Scientific CMOS cameras (Photometrics). CFP of the ATP FRET-based biosensors was excited with 435 nm LED light (CoolLED pE-800). Image analysis was performed with Fiji software. Images were background subtracted and thresholded with the Triangle method before automatic assessment of the insensities of thresholded CFP and FRET images.

For ATP measurement in BMDMs, retrovirus was generated by combining 1.5 μg of the viral plasmid (MSCV Puro backbone with AT1.03 or mtAT1.03) and 1.5 μg of the pCl-Eco retroviral capsid plasmid in 400 μl of antibiotic-free, serum-free RPMI1640 medium. To this mixture, 7.5 μl of TransIT transfection reagent was added and incubated (30 min, RT). The transfection complex was then added dropwise to the HEK cells, with the plate gently shaken. After 48 h, the virus-containing supernatant was harvested and mixed with 106 bone marrow cells per 6-well to a final volume of 2 ml per well. Spin infection was performed (45 min, 1200 gn, RT, low brake setting [3-4]). After 4 days of differentiation in BMDM medium, the infected cells were reseeded in 6 cm culture dishes for imaging.

Cells were treated as indicated and ATP measurements were performed using a wavelength of 840 nm to excite mseCFP and cp173-mVenus fluorescent proteins. The emission signals were collected simultaneously in cyan and yellow channels using emission barrier filter pairs (bandwidth of 455–490 nm and 526–557 nm) on the Olympus MPE-resonant scanner system. Image analysis was performed with IMARIS software with background subtracted and thresholded before automatic assessments.

Metabolic analysis

Oxygen consumption rates (OCR) and extracellular acidification rates (ECAR) were measured by extracellular flux analysis with a Seahorse XFe96 Analyzer (Agilent). One day before the experiment, HCT116 cells or BMDMs were plated to Xfe cell culture micro-plates at a density of 2×10^4 or 7×10^4 cells per well, respectively. On the day of the experiment, the cell culture medium was exchanged to bicarbonate- and phenol red-free seahorse base medium supplemented with 2 mM L-glutamine, 10 mM glucose, and 5 mM HEPES (pH 7.4) or XF RPMI medium, pH 7.4, supplemented with 1 mM pyruvate, 2 mM L-glutamine, and 10 mM glucose for HCT116 or BMDMs, respectively. The cells were incubated at 37°C in a CO_2-free incubator for 1 h. Compounds were diluted in seahorse base medium and injected as indicated. Measurements were performed in quadruplicates. ATP was neutralized to pH 7.4, and the measurements of ATP injections in wells without cells served as background correction wells to account for pH changes caused by ATP. Data analysis was performed using Wave software (Agilent, Version 2.6.1) and data is baselined to the last measurement before compound administration.

Metabolomics

BMDMs from Pycard$^{-/-}$ mice were harvested on day 6 of cultivation, seeded in 53 mm non-cell culture-treated dishes at a density of 5.5×10^6 cells per dish and incubated overnight. A range-finder experiment to optimize the cell number per condition for untargeted metabolomics analysis also included samples from 6-well plate wells (2.3×10^6 cells) and 10 cm dishes (15×10^7 cells) (Figure S4A). At the day of experiment, cells were primed with 50 ng ml^{-1} LPS and subsequently stimulated with 5 μM nigericin, 2.5 μM FCCP, or 2.5 mM ATP, or medium for 1 h. All treatments were performed in quadruplets. Cell lysates were prepared on ice by removing cell supernatants and washing with an equal volume of cold 0.9% NaCl solution. NaCl was removed and 2 ml ice-cold lysis buffer (Metabolon RS4 standard at a concentration of 3.125 μg ml^{-1} in 80% methanol) was added. Cells were scraped off and transferred to 2 ml LC-MS glass vials with screw caps. Solvent was removed by drying the samples under warm (<=40 °C) N_2 and samples were shipped to Metabolon, Inc. (Morrisville, NC, USA).

Metabolomics quantification was performed using non-targeted ultra-high performance liquid chromatography-tandem mass spectrometry (UPLC-MS/MS) methods, which included both compound identification and relative quantification processes. The

sample preparation and mass detection procedures were executed in accordance with the previously published technical proposal.[86] Quality control in the Metabolon platform included: technical replicates, pooled matrix samples originating from experimental sample to ensure robustness; blanks, extracted water sample to account for background interference; QC standards, meticulously selected standards added into each analyzed sample to allow instrument performance monitoring and aide chromatographic alignment. A Waters ACQUITY UPLC and a Thermo Scientific Q-Exactive high resolution/accurate mass spectrometer with a heated electrospray ionization (HESI-II) source and Orbitrap mass analyzer at 35,000 mass resolution were used. The UPLC methods were optimized for hydrophilic and hydrophobic molecules and the mass analyzer applied in positive and negative modes for four UPLC-MS/MS methods per sample. The scan range varied slightly between methods, but covered 70 to 1000 $m\ z^{-1}$. The metabolomics identification was facilitated by software developed by Metabolon, based on an internal library with authenticated standards including the retention time/index (RI), mass to charge ratio ($m\ z^{-1}$), and chromatographic data (including MS/MS spectral data). The quantification of each peak was determined using the area under the curve.

Statistical analysis of metabolomics data was conducted using the R programming language, employing a custom-built data analysis pipeline developed in-house. After quality check, keeping all data, the analysis yielded a dataset comprising 570 metabolites across 36 samples. Missing values for each metabolite were imputed using the minimum value across the median-scaled data. The batch-norm-imputed data was natural log transformed and then used for data analysis. Principal component analysis (PCA) was employed to reduce the dimension of the selected data. The two-sample t-test with equal variance was used to assess the differences between the experimental groups. To account for multiple testing, the Benjamini–Hochberg false discovery rate (FDR) procedure was applied to all p-values within each comparison. The statistical significance level was set at 0.05. For visualization of changes in metabolite levels upon treatments, volcano plots were used. Significantly different metabolites were subsequently subjected to pathway enrichment analysis using MBROLE 3.0,[87] focusing on enriched pathways contained in the HMDB and KEGG databases. The term 'Metabolic pathways' was excluded from the displayed panels. Significantly enriched pathways were sorted based on count size, followed by a decreasing $-\log_{10}$(FDR).

Xenopus animal experiments
Xenopus *compound treatment*
Xenopus embryos were treated as indicated at stage 39/40 (16 h, 16°C, protected from light). Ten embryos per well were incubated in 24-well plates containing 2 ml of the indicated drug in 1/3 Modified Ringers solution (MR) + Gentamycin.
Xenopus *TUNEL staining*
After treatment, embryos were fixed in MEMFA overnight at 4°C and stored in 100% ethanol at -20°C until use. Embryos were bleached before staining. TUNEL staining was performed according to the manufacturer's protocol using terminal deoxynucleotidyl transferase (Invitrogen), dig-UTP (Roche), anti-digoxigenin AP antibody (Roche), and NBT/BCIP (Roche). Samples were stopped using methanol, rehydrated, and fixed with 4% PFA in PBS. TUNEL positive cells were counted using images enhanced for brightness and contrast in ImageJ and the cell counter plugin. To avoid bias due to uneven staining, the stronger stained side in each embryo was quantified.
Xenopus *imaging*
TUNEL-stained embryos were washed with PBS (3x, 15 min), followed by PBS supplemented with 0.1% Triton X-100 (2x 30 min), and blocked with PBS supplemented with 0.1% Triton X-100 and 10% CAS blocking (Thermo Fisher Scientific) for 1 h at RT. Samples were stained with primary anti-acetylated-α–tubulin mAB (Sigma, #T6793) overnight at 4°C and secondary AlexaFluor 488-labeled goat anti-mouse antibody (Invitrogen, #A11001) for 2 h at RT In 100% CAS blocking. Whole embryo bright-field images were taken on a Zeiss Stemi508 and Axiocam 208 Color setup, and immunofluorescent images with a Zeiss Discovery V8 with a Axiocam 305 Color and Zeiss Zen Pro Blue software. Brightfield images were adjusted for color balance, brightness and contrast, and fluorescent images were adjusted for brightness and contrast using ImageJ.

QUANTIFICATION AND STATISTICAL ANALYSIS

Statistical analysis
For continuous observations, a paired or unpaired t-test, or a minimal effect test (MET) was applied to test for significant effects, as indicated in the figure legends. Two-tailed t-tests were applied to test the null hypothesis. A two-sample F-test was applied to test for unequal variances and to decide whether a t-test with equal, or unequal variances (Welch's test) was more appropriate. Unequal variances were assumed if the F-test was significant with p<0.05. METs were performed with a 20% difference of the larger mean as threshold and responses that did significantly reject the hypothesis of such a minimal difference were considered as essentially intact. To minimize multiple testing issues, only biologically prespecified hypotheses were tested. If multiple tests were applied to a single data set, the Bonferroni-Holm correction was applied to adjust p-values and thereby prevent inflation of the family-wise error rate. Statistical significance is indicated with asterisks: *$p < 0.05$; **$p < 0.01$; ***$p < 0.001$; and n.s., not significant.

Half-maximal doses $x_{50,}$ which can be interpreted as IC_{50}, EC_{50}, or ET_{50} depending on the context, were estimated using maximum likelihood estimation based on a hill function $F(x) = F_0 + F_{max} * x^h/(x_{50}^h + x^h)$ with four parameters F_0, F_{max}, h and x_{50}. In this equation x_{50} is the value x where the observation $F(x)$ is in the middle of the estimated baseline F_0 and the estimated maximum F_{max}. If percentage data was analyzed, we were interested in the x-value where 50% is reached. This value is calculated by solving F(x)=50% for

x after estimating all four parameters. 95% confidence intervals were calculated using the profile likelihood approach to account for non-linearity of the equation. The likelihood ratio test was applied to test whether x_{50} is different in two experimental conditions.

All tests were performed using MATLAB (The Mathworks Inc., v 9.11.0.1769968 [R2021b]). The type of test applied to the respective data set is indicated in the figure legends.

Statistical analysis of metabolomics data is separately outlined in the respective paragraph.

Replicates and data depiction

The number of replicates per experiment is indicated in the respective figure legend.

Unless indicated otherwise, data with error bars show mean±SD. The respective figure legends indicate if mean/SEM ±SD of technical replicates of one independent experiment or if mean±SD of combined data of several independent experiments is shown.

Quantifications

Quantifications of immunoblots were done as described in the respective paragraph.